Check for updates

A New Class of Cell Wall-Recycling L,D-Carboxypeptidase Determines β-Lactam Susceptibility and Morphogenesis in *Acinetobacter baumannii*

Yunfei Dai,[a] Victor Pinedo,[b] Amy Y. Tang,[a] Felipe Cava,[b] Edward Geisinger[a]

[a]Department of Biology, Northeastern University, Boston, Massachusetts, USA
[b]Laboratory for Molecular Infection Medicine Sweden, Department of Molecular Biology, Umeå Centre for Microbial Research, Umeå University, Umeå, Sweden

ABSTRACT The hospital-acquired pathogen *Acinetobacter baumannii* possesses a complex cell envelope that is key to its multidrug resistance and virulence. The bacterium, however, lacks many canonical enzymes that build the envelope in model organisms. Instead, *A. baumannii* contains a number of poorly annotated proteins that may allow alternative mechanisms of envelope biogenesis. We demonstrated previously that one of these unusual proteins, ElsL, is required for maintaining a characteristic short rod shape and for withstanding antibiotics that attack the septal cell wall. Curiously, ElsL is composed of a leaderless YkuD-family domain usually found in secreted, cell wall-modifying L,D-transpeptidases (LDTs). Here, we show that, rather than being an LDT, ElsL is actually a new class of cytoplasmic L,D-carboxypeptidase (LDC) that provides a critical step in cell wall recycling previously thought to be missing from *A. baumannii*. Absence of ElsL impairs cell wall integrity, morphology, and intrinsic resistance due to buildup of murein tetrapeptide precursors, toxicity of which is bypassed by preventing muropeptide recycling. Multiple pathways in the cell become sites of vulnerability when ElsL is inactivated, including L,D-cross-link formation, cell division, and outer membrane lipid homoeostasis, reflecting its pleiotropic influence on envelope physiology. We thus reveal a novel class of cell wall-recycling LDC critical to growth and homeostasis of *A. baumannii* and likely many other bacteria.

IMPORTANCE To grow efficiently, resist antibiotics, and control the immune response, bacteria recycle parts of their cell wall. A key step in the typical recycling pathway is the reuse of cell wall peptides by an enzyme known as an L,D-carboxypeptidase (LDC). *Acinetobacter baumannii*, an "urgent-threat" pathogen causing drug-resistant sepsis in hospitals, was previously thought to lack this enzymatic activity due to absence of a known LDC homolog. Here, we show that *A. baumannii* possesses this activity in the form of an enzyme class not previously associated with cell wall recycling. Absence of this protein intoxicates and weakens the *A. baumannii* cell envelope in multiple ways due to the accumulation of dead-end intermediates. Several other organisms of importance to health and disease encode homologs of the *A. baumannii* enzyme. This work thus reveals an unappreciated mechanism of cell wall recycling, manipulation of which may contribute to enhanced treatments targeting the bacterial envelope.

KEYWORDS *Acinetobacter*, L,D-carboxypeptidase, antibiotic resistance, cell wall recycling, morphology, peptidoglycan

The Gram-negative pathogen *Acinetobacter baumannii* is a significant cause of health care-associated infections, including ventilator-associated pneumonia, bloodstream infections, urinary tract infections, and sepsis (1, 2). *A. baumannii* strains show widespread multidrug resistance, limiting the number of therapies effective against such infections (3).

This problem is compounded by the insufficient pipeline of new antibiotics active against Gram-negative pathogens (4). Reflecting the urgency of this threat, the World Health Organization has ranked *A. baumannii* as a pathogen of highest priority for research and development of new antibiotics (4).

The distinct cell envelope of *A. baumannii* is a key potential target for new treatments, but many aspects of its synthesis and control are not understood. Building the critical peptidoglycan (PG) cell wall layer, in particular, appears to involve several unconventional and poorly defined strategies. A number of proteins integral to the canonical pathways of septal PG synthesis, cell separation, and PG recycling have no homologs in the microorganism (5). For instance, *A. baumannii* lacks an ortholog of *Escherichia coli* LdcA or *Vibrio cholerae* LdcV, L,D-carboxypeptidases (LDCs) necessary for reusing peptides derived from old PG for synthesis of new cell wall (6, 7).

In addition to lacking canonical enzymes, the pathogen encodes several proteins that are implicated in PG homeostasis based on domain annotations but whose actual functions remain mysterious (5). Prominent among this group are two YkuD-domain proteins, which we have named ElsL (ACX60_RS03475) and Ldt$_{Ab}$ (ACX60_RS05685) (5) (referred to as LdtK and LdtJ in reference 8). YkuD domains are found in secreted enzymes that modify the cell wall for a variety of purposes in other organisms (9). For example, many YkuD-domain proteins carry out L,D-transpeptidase (LDT) reactions that generate 3-3 cell wall cross-links. These bonds are usually less abundant than the 4-3 cross-links catalyzed by DD-transpeptidases (penicillin binding proteins [PBPs]) but may reinforce the wall against envelope stress (9). Unlike PBPs, LDTs are generally insensitive to β-lactam antibiotics (with the exception of carbapenems), and thus LDTs have been implicated in contributing to drug resistance (10, 11). Ldt$_{Ab}$, but not ElsL, was recently found to be essential for 3-3 cross-links (8). Interestingly, ElsL does not contain a detectable secretion signal or additional domains such as PG binding motifs that would target the protein to the cell wall (5). Functional predictions based on identification of conserved domains in ElsL are therefore limited. A few leads were obtained based on genome-wide profiling of antibiotic susceptibility phenotypes (5). These studies found that ElsL deficiency is closely related to malfunction of the Rod system, the multiprotein PG synthetic machinery responsible for cell elongation. Mutations affecting ElsL and the Rod system both caused hypersensitivity to the same subset of β-lactam antibiotics as well as dramatic loss of the bacterium's characteristic short rod shape (5). ElsL mutation was also associated with increased outer membrane (OM) shedding (8). The role ElsL plays in the cell and its link to Rod system function and the OM remain unknown.

In this paper, we have determined the function of ElsL in *A. baumannii* cell wall synthesis. We show that ElsL defines a novel, noncanonical class of cytoplasmic LDC essential to cell wall recycling. We have identified critical perturbations to cell wall metabolism and integrity that occur in the absence of this function. We also delineated the complete network of genetic interactions with *elsL*, revealing multiple cellular pathways that are affected by its inactivation.

RESULTS

ElsL and Ldt$_{Ab}$ have opposing effects on L,D-cross-link formation in *A. baumannii*. To determine the effect of the two *A. baumannii* YkuD-family proteins, ElsL and Ldt$_{Ab}$, on modifying the cell wall, we analyzed deletion mutants using two assays that detect PG remodeling: (i) metabolic cell wall labeling using the fluorescent precursor HCC-amino D-alanine (HADA), incorporation of which depends on an exchange reaction catalyzed by transpeptidases, including LDTs (12), and (ii) analysis of cell wall muropeptide composition by ultraperformance liquid chromatography-mass spectrometry (UPLC-MS) (13).

Wild-type (WT) bacteria incubated with HADA incorporated the label throughout their cell walls, with the population of dividing cells showing increased signal at the midcell (Fig. 1A and B). Deletion of *ldt*$_{Ab}$ resulted in a dramatic loss of signal along the side-wall of cells that was reversed by reintroducing the gene in *trans* (Fig. 1A to D). In contrast, deletion of *elsL*, while causing loss of the short rod shape, caused no decrease
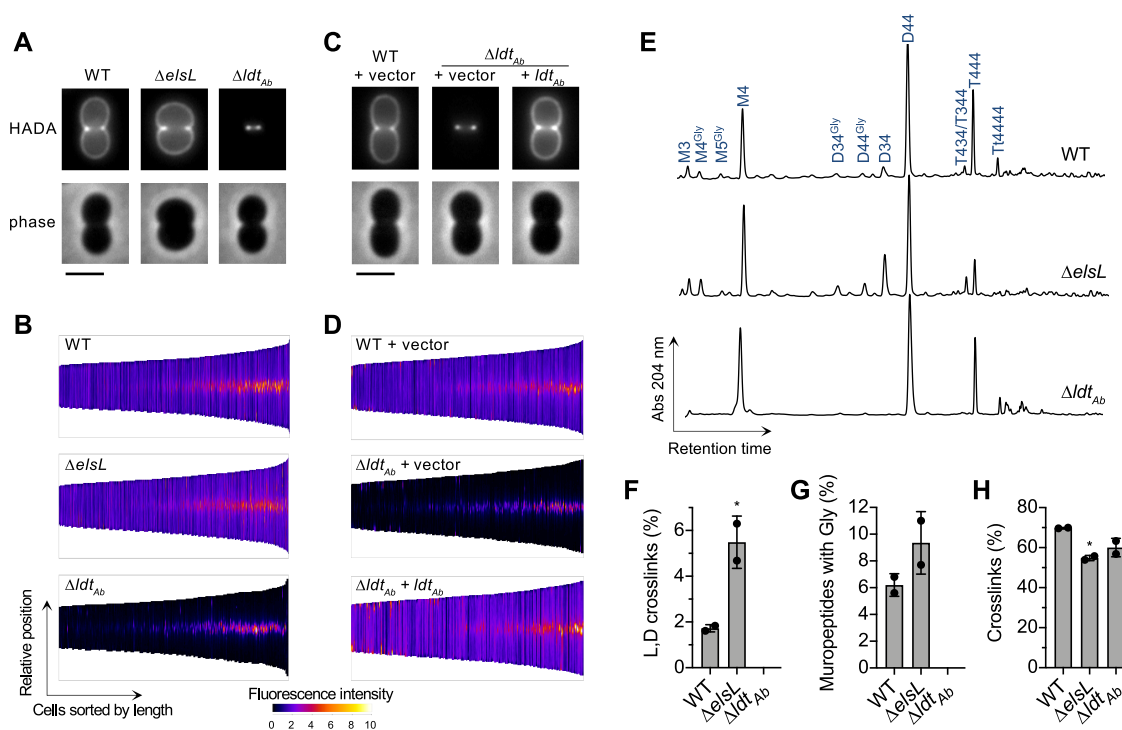
FIG 1 ElsL and Ldt$_{Ab}$ have opposing effects on L,D-cross-link formation. (A and C) Cells of the indicated *A. baumannii* strains were metabolically labeled with HADA and imaged by fluorescence and phase-contrast microscopy. Representative cells are shown. Scale bar, 2 μm. (B and D) Demographic representation of the cellular distribution and intensity of the HADA label. Cells ($n \geq 227$ with each strain) were ordered according to their length and stacked by aligning cell midpoints. Fluorescence intensity along the medial axis of each cell is displayed as a heat map. (E) Muropeptide profile analysis. Major muropeptides and those showing differences between the WT and mutant are labeled. "M" indicates monomeric muropeptide; "D," "T," and "Tt" indicate dimeric, trimeric, or tetrameric cross-linked muropeptides, respectively; number(s) indicate the residue length of the stem peptide(s). "Gly" indicates that the terminal residue is a glycine. (F to H) The percentage of L,D-cross-links, glycine-containing muropeptides, and total cross-linked muropeptides were quantified. Bars show the mean $\pm$ standard deviation (SD) ($n = 2$ biological replicates). *, $P < 0.05$ in unpaired t test comparing $\Delta elsL$ versus WT (F and G) or in one-way analysis of variance (ANOVA) with Dunnett's multiple-comparison test comparing each mutant to the WT (H).

in HADA incorporation (Fig. 1A and B). These phenotypes confirm previous findings with a related fluorescent label (8). The Δldt_{Ab} phenotype also resembled that seen with *E. coli* completely lacking its 6 LDT paralogs (14).

Cell wall muropeptide profiling revealed changes consistent with the metabolic labeling experiments. The WT profile consisted of major and minor muropeptide peaks similar to those reported previously (Fig. 1E) (15–18). Deletion of ldt_{Ab} caused complete loss of LDT-generated muropeptides, including the D34 (L,D-cross-linked) dimer (Fig. 1E and F) and muropeptides containing a terminal glycine (fourth position) residue from D-alanine exchange (Fig. 1E and G), consistent with prior findings (8). In stark contrast, the $\Delta elsL$ strain showed an increase in the L,D-cross-linked D34 muropeptide compared to the WT (Fig. 1E and F; Fig. S1). Muropeptides with terminal glycines also appeared to increase in the $\Delta elsL$ mutant (Fig. 1E), although their overall levels were not significantly different from the WT based on unpaired t test results (Fig. 1G). The biological significance of these glycine residues in *A. baumannii* or other organisms (19, 20) is not well defined. Despite the increase in 3-3-cross-links, the $\Delta elsL$ cell wall showed lower total cross-linkage (including 4-3 as well as 3-3 bonds; Fig. 1H). Taken together, these data confirm that Ldt$_{Ab}$ is the LDT responsible for alternative cross-linking within the *A. baumannii* cell wall and indicate that ElsL is not a canonical LDT. Rather, ElsL has an alternative function that influences both 4-3 and 3-3 cross-link formation as well as cell shape.

Analysis of fluorescent protein fusions supports the prediction that ElsL function is cytosolic. Fusion of ElsL to a monomeric superfolder green fluorescent protein (GFP) (msGFP2 [21]) caused a diffuse signal throughout the cell interior, consistent with
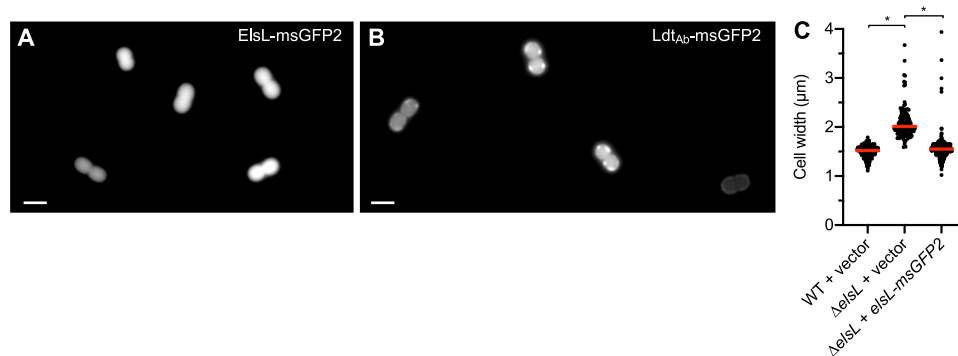
FIG 2 An ElsL-msGFP fusion shows diffuse cytoplasmic localization, while Ldt$_{Ab}$-msGFP localizes to the cell periphery. (A and B) Fluorescent micrographs showing representative WT cells harboring the plasmid-borne gene fusions of msGFP2 to *elsL* (A) or *ldt$_{Ab}$* (B). Scale bar, 2 μm. (C) The *elsL-msGFP2* fusion reverses the morphology defect of $\Delta elsL$. Cells were imaged by phase-contrast microscopy, and cell width was measured by image analysis. Bars show median values ($n \geq 118$). *, $P < 0.0001$ in Kruskal-Wallis test.

cytoplasmic localization (Fig. 2A). An analogous Ldt$_{Ab}$-msGFP2 fusion, in contrast, showed peripheral fluorescent patches consistent with its predicted localization in the periplasm (Fig. 2B). This difference in localization occurred despite both gene fusions resulting in similarly efficient levels of intact chimeric proteins (Fig. S2A). Expression of *elsL-msGFP2* reversed the shape defect of $\Delta elsL$ bacteria, resulting in short rods with maximal width matching that of the WT, indicating that the fusion protein was functional (Fig. 2C). With a cytoplasmic location partitioned away from the sacculus, ElsL may thus act as an LDC, an alternative or additional activity seen with some YkuD-family proteins (22, 23). The logical extension of this prediction is that ElsL is the missing-link cytoplasmic LDC allowing recycling of imported cell wall fragments in *A. baumannii*.

elsL and ldt$_{Ab}$ have interconnected aggravating genetic interactions. As a parallel approach to identify leads on ElsL function, we mapped its full network of genetic interactions throughout the genome, which ultimately enabled a series of tests of the above-described hypothesis. To this end, we performed comparative transposon insertion sequencing (Tn-seq) analysis using ElsL$^+$ and ElsL$^-$ strains. A dense *mariner* transposon library was constructed in the $\Delta elsL$ background, and colony growth of the resulting double mutants was quantified in massively parallel fashion by measuring Illumina sequencing read abundance corresponding to every member of the library (Materials and Methods). This growth was then compared to that of the matching single (ElsL$^+$) transposon mutants within a control *mariner* library generated previously in the WT (5). Potential aggravating interactions were identified as genes for which knockout showed growth dependence on ElsL (i.e., a low ratio of $\Delta elsL$/control read counts), with significance determined by permutation test. Examination of such interactions should illuminate the pathways in which ElsL functions.

A large number of genes showed potential aggravating interactions with *elsL* (Fig. 3A, left; Data Set S1). Several of these mapped to cell wall synthesis, cell division, and envelope stability pathways. For example, the nonessential cell division-associated genes *minCD*, *blhA* (5, 24), and ACX60_RS13190 (structural maintenance of chromosomes family [5]) showed substantially lower Tn-seq read counts when mutated in combination with $\Delta elsL$ (Fig. 3A and B). A similar result was seen with *zapA*, a cell division locus linked to *RS13190*, albeit without passing the 5% false-discovery rate cutoff (Fig. 3A and B). In addition, nearly all *mla* genes, which play a role in lipid transport between the OM and inner membrane (IM) (25, 26), had Tn-seq read counts dependent on intact *elsL* (Fig. 3A and B). Notably, *ldt$_{Ab}$* also showed a prominent growth defect dependent on $\Delta elsL$ (Fig. 3A and B), indicating that knockout of both YkuD-family proteins was poorly tolerated in *A. baumannii*, as suggested previously (8). To interrogate this last result, we generated a parallel *mariner* library in the Δldt_{Ab} strain and analyzed its genome-wide interactions (Data Set S2). While many fewer potential negative interactions were identified with Δldt_{Ab} than with $\Delta elsL$, the strongest hit
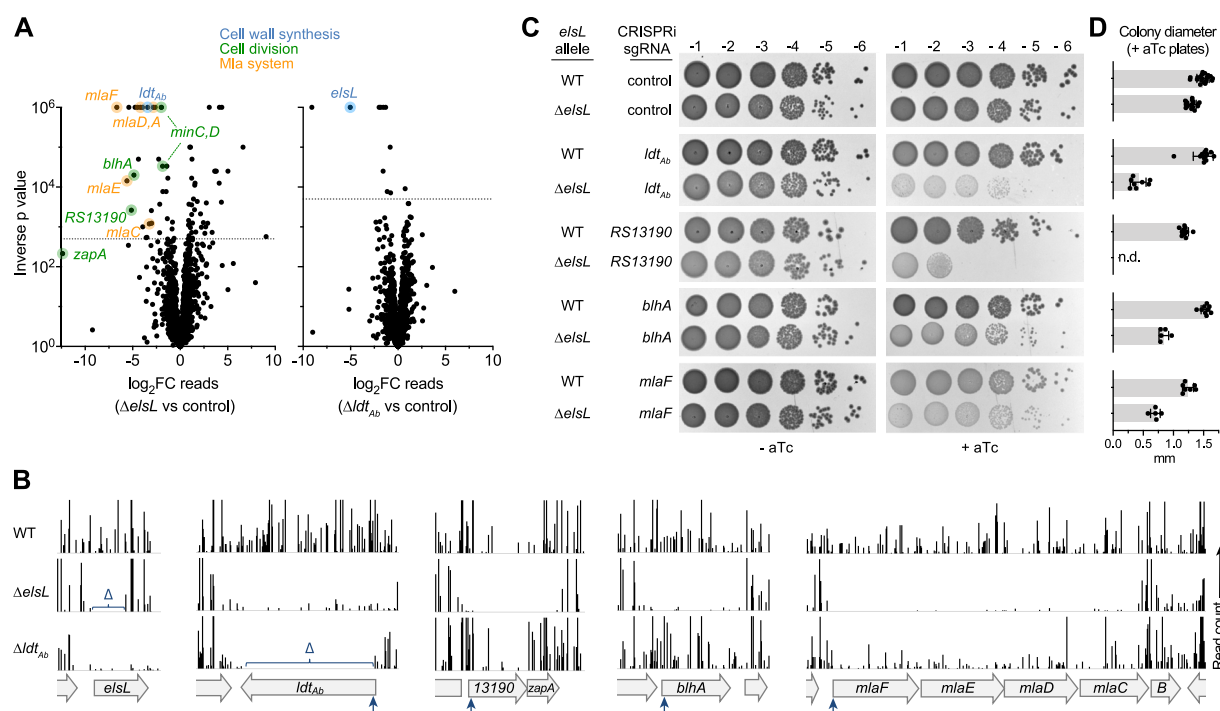
FIG 3 Tn-seq reveals aggravating genetic interactions with *elsL* and *ldt*Ab. (A) Tn-seq genetic interaction analysis. Volcano plot shows the ratio of Tn-seq read counts mapped to genes in the mutant *mariner* transposon library (Δ*elsL* or Δ*ldt*Ab) compared to the control transposon library (WT). Dotted horizontal lines indicate a false-discovery rate (*q* value) of 0.05. Hits described in the text are color-highlighted according to the indicated pathway. (B) Tracks show Tn-seq read counts at each insertion site at different chromosomal loci within the indicated *mariner* library. Bars represent the normalized read count, and vertical arrows indicate the position targeted by CRISPRi. Δ indicates a deleted region. (C) Validation of aggravating genetic interactions with Δ*elsL* via targeted CRISPRi and colony formation tests. WT or Δ*elsL* strains harboring aTc-inducible *dcas9* and the indicated sgRNA were serially diluted (10-fold) and spotted on LB agar medium supplemented with 0 or 50 ng/mL aTc. Colonies resulting after overnight 37°C incubation were imaged. (D) Diameters of colonies from triplicate aTc plates at 10^{-6} or higher dilution were measured by image analysis. Bars show the mean ± SD (*n* ≥ 5 colonies). *P* < 0.0001 in unpaired *t* tests comparing Δ*elsL* to WT with each sgRNA. n.d., colonies not detected and statistical test not performed.

was *elsL* (Fig. 3A, right; Fig. 3B; Data Set S2), supporting the notion that the two genes have an aggravating interaction.

We used CRISPR interference (CRISPRi) (27) to validate the negative genetic interactions between *elsL* and the strongest hits within each pathway (*ldt*Ab, *RS13190-zapA*, *blhA*, and *mlaC-F*). Chimeric single guide RNAs (sgRNAs) were designed to target the 5′ end of each locus (Fig. 3B, blue arrows) and were introduced into WT and Δ*elsL* strains harboring anhydrotetracycline (aTc)-inducible dCas9. CRISPRi allows efficient knockdown of operons (28); *RS13190-zapA* and *mlaC-F* are therefore each likely to be corepressed in this strategy. The effect of knockdown on colony growth was compared with two parallel controls—(i) growth in the absence of dCas9 inducer (− aTc) and (ii) growth with a control, nontargeting sgRNA (27). CRISPRi of each locus in the WT strain resulted in colony growth that was at or near control levels (Fig. 3C and D). In contrast, CRISPRi in Δ*elsL* caused greatly amplified growth defects. Silencing *RS13190* in the Δ*elsL* background completely blocked colony formation (Fig. 3C and D), indicative of strong genetic aggravation. Other knockdowns in Δ*elsL* resulted in significantly reduced colony growth compared to controls (Fig. 3C and D). To test whether these growth defects reflect aggravating interactions with *elsL*, we compared them to those expected from a null multiplicative model based on the growth of single-lesion strains (Materials and Methods). Each double-lesion strain (CRISPRi + Δ*elsL*) had significantly lower growth than expected from the null model (Table S1). Together, these results indicate that *elsL* interacts negatively with LDT, cell division, and OM lipid transport pathways.

Aggravating interactions frequently arise if the underlying genes function in parallel or redundant pathways (29). This scenario could explain the basis for the aggravating
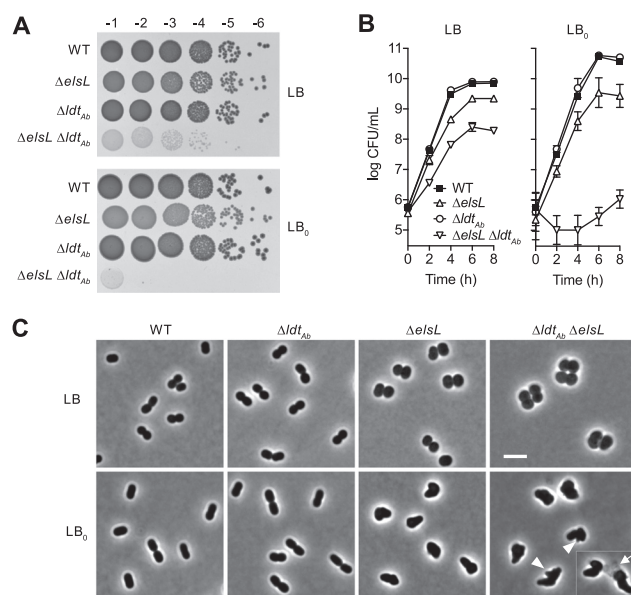
FIG 4 Synthetic lethal interaction between *elsL* and *ldt*$_{Ab}$. (A) WT *A. baumannii* or the indicated deletion mutant were serially diluted and spotted on LB (top) or LB$_0$ (bottom) agar medium, and the resulting colonies were imaged as in Fig. 3. (B) The indicated strains were cultured to saturation in LB and diluted in LB or LB$_0$, and viable counts were determined over time. Data points show the geometric mean ± SD (*n* = 3 biological replicates). Where not visible, error bars are within the confines of the symbol. (C) The indicated strains (columns) cultured in LB or LB$_0$ (rows) were imaged by phase-contrast microscopy. Arrowheads indicate blebs; the arrow indicates an example of a lysed cell lacking dense phase contrast. Scale bar, 4 μm.

interaction between *elsL* and nonessential cell division genes. Mutation of *blhA* (24) and silencing of *RS13190-zapA* (Fig. S3A) each impair cell division and cause a mode of growth that is more heavily dependent on cell elongation compared to the WT. Loss of *elsL* causes loss of short rod shape and is phenotypically linked to malfunction of the cell elongation machinery (5) (Fig. 2C). Blocking genes of each type in combination may thus result in cells being unable to divide or elongate efficiently. This is supported by microscopy of Δ*elsL* CRISPRi$_{RS13190-zapA}$, which showed large, irregular spheroid morphology rather than the filaments seen with CRISPRi$_{RS13190-zapA}$ alone (Fig. S3A). These data are consistent with synthetic lethality occurring due to an inability of cells to continue growing their cell wall laterally as a way to compensate for deficient or delayed cell division. Defective elongational growth machinery could also affect how septal PG synthesis is initiated (30, 31), hypersensitizing to inhibition of a parallel cell division pathway. In addition to parallel pathways, aggravating interactions may arise when one gene product limits the toxicity generated by the absence of the other (32–34). We considered this alternative model in examining the mechanism of the *elsL-ldt*$_{Ab}$ genetic interaction.

Synthetic lethal relationship between *elsL* and *ldt*$_{Ab}$. To investigate the *elsL-ldt*$_{Ab}$ genetic relationship, we combined the two deletions (Materials and Methods) and identified conditions that further aggravate its growth phenotype. The Δ*elsL* Δ*ldt*$_{Ab}$ double mutant formed small, translucent colonies, identical to the phenotype of the Δ*elsL* CRISPRi$_{ldtAb}$ strain (Fig. 4A). Since both genes affect the cell wall, we examined growth with low osmolarity medium (LB without NaCl, "LB$_0$"). LB$_0$ medium dramatically aggravated the Δ*elsL* Δ*ldt*$_{Ab}$ growth defect, with colony formation completely blocked at dilutions beyond 10^{-2}, indicating synthetic lethality (Fig. 4A). A similar result was obtained with Δ*elsL* CRISPRi$_{ldtAb}$ (Fig. S3B). Consistent with the colony phenotypes, Δ*elsL* Δ*ldt*$_{Ab}$ showed lower viable counts during liquid culture compared to the single mutants and WT, with low osmolarity amplifying the defect (Fig. 4B). The Δ*elsL* Δ*ldt*$_{Ab}$ sacculus showed compositional defects that reflected the combination of each single lesion, with low overall cross-linking and absence of LDT-mediated muropeptides

(Fig. S3C and D). The detrimental effect of lacking both genes also manifested in defective cell shape, with the double mutant forming enlarged spheroids in LB and irregular, bloated shapes with frequent blebs and lysis in LB_0 (Fig. 4C). Notably, the $\Delta elsL$ single mutant also had viability and shape defects compared to the WT that were exacerbated by low osmolarity, while Δldt_{Ab} was unaffected (Fig. 4B and C), underlining the importance of ElsL to physiology and stress resistance. Together, these results indicate that $elsL$ and ldt_{Ab} have a synthetic lethal relationship, with the $elsL$ defect, in particular, making cells sensitive to conditions of increased cell wall stress.

Suppression of $elsL$-ldt_{Ab} synthetic lethality by blocking cell wall muropeptide recycling. To illuminate ElsL function and identify the source of $\Delta elsL$ toxicity, we exploited the synthetic lethality of $\Delta elsL$ Δldt_{Ab} and isolated suppressor mutants reversing its major growth defect. Large, opaque colonies forming from $\Delta elsL$ Δldt_{Ab} on solid LB or LB_0 medium were purified and their mutations mapped (Materials and Methods). Of 22 distinct suppressors identified using this strategy, 21 mapped to 2 genes functioning in PG recycling, $ampG$ (the muropeptide permease) and mpl (murein peptide-UDP-MurNAc ligase) (35) (Fig. 5A). In each case, the mutation was a predicted null allele. Representative mutants showed enhanced colony growth with both LB and LB_0 (Fig. 5B), as did an independently constructed, in-frame deletion of $ampG$ (Fig. 5C). The remaining suppressor, which also enhanced colony growth relative to its parent (Fig. 5B), mapped to ACX60_RS13100, which we have named $ltgF$ (lytic transglycosylase determining fosfomycin susceptibility, as explained below). This locus encodes a predicted lytic transglycosylase having an MltD-like catalytic domain and a large C-terminal region with multiple LysM repeats resembling the PG-anchoring domain of autolysins (Fig. 5D) (36). The mutant allele had an insertion sequence (IS) between these two regions. As a predicted PG turnover enzyme, $ltgF$ may have an important role in PG recycling like the other sites of suppression. Supporting this idea, the Tn-seq antibiotic susceptibility profile (phenotypic signature) (5) of $ltgF$ closely correlates with those of canonical PG-recycling genes (Fig. 5E, Fig. S4A). In-frame deletion of $ltgF$ in ATCC 17978 (Fig. 5F and G) as well as transposon mutation in a different strain background (AB5075, Fig. S4C, D) each caused hypsersusceptibility to fosfomycin, a mark of defective cell wall recycling (37, 38). The susceptibility defect was akin to that seen with recycling-blocked $ampG$ mutants tested in parallel (Fig. 5F and G, Fig. S4C and D). Among predicted lytic transglycosylases in *A. baumannii*, LtgF is the only one with a Tn-seq phenotypic signature showing significant positive correlation with cell wall recycling (Fig. S4B) and characterized by significant hypersensitivity to fosfomycin (5). The above-described results support a role for $ltgF$ in PG turnover and recycling. The findings altogether reveal that the $\Delta elsL$ Δldt_{Ab} growth defect is suppressed by blocking cell wall recycling at key points—its earliest steps (generation of anhydromuropeptides or their import) or at the step of peptide reuse (Fig. 5I, left, bold steps).

Reexamination of our genetic interaction Tn-seq data revealed that blocking the same cell wall-recycling steps identified as suppressors of $\Delta elsL$ Δldt_{Ab} lethality also alleviated the mild colony growth defect of $\Delta elsL$. For instance, transposon mutations in $ltgF$ and cell wall-recycling enzymes acting on muropeptide or peptide substrates (Fig. 5I) each led to slightly enhanced growth within the $\Delta elsL$ library compared to the control (Fig. 5H). In contrast, mutation of other recycling steps dedicated to MurNAc sugar recycling had the opposite effect, decreasing $\Delta elsL$ growth compared to the control (Fig. 5H). A clear differential effect of blocking different branches of the cell wall recycling circuit on growth was not observed with the Δldt_{Ab} library (Fig. S4E). These results point to ElsL deficiency and peptide reuse as the key sources of synthetic toxicity that are bypassed by cell wall recycling block.

The suppressor analysis clearly implicates ElsL in cell wall recycling. Integrated with our genetic interaction, muropeptide composition, and localization data, these results lend strong support for the above-described model that ElsL is the cell wall-recycling LDC in *A. baumannii*. The deleterious effects of ElsL deficiency can thus be explained as a consequence of aberrant buildup of its tetrapeptide substrates. Processing of these intermediates by Mpl and other enzymes would lead to generation of lipid-II
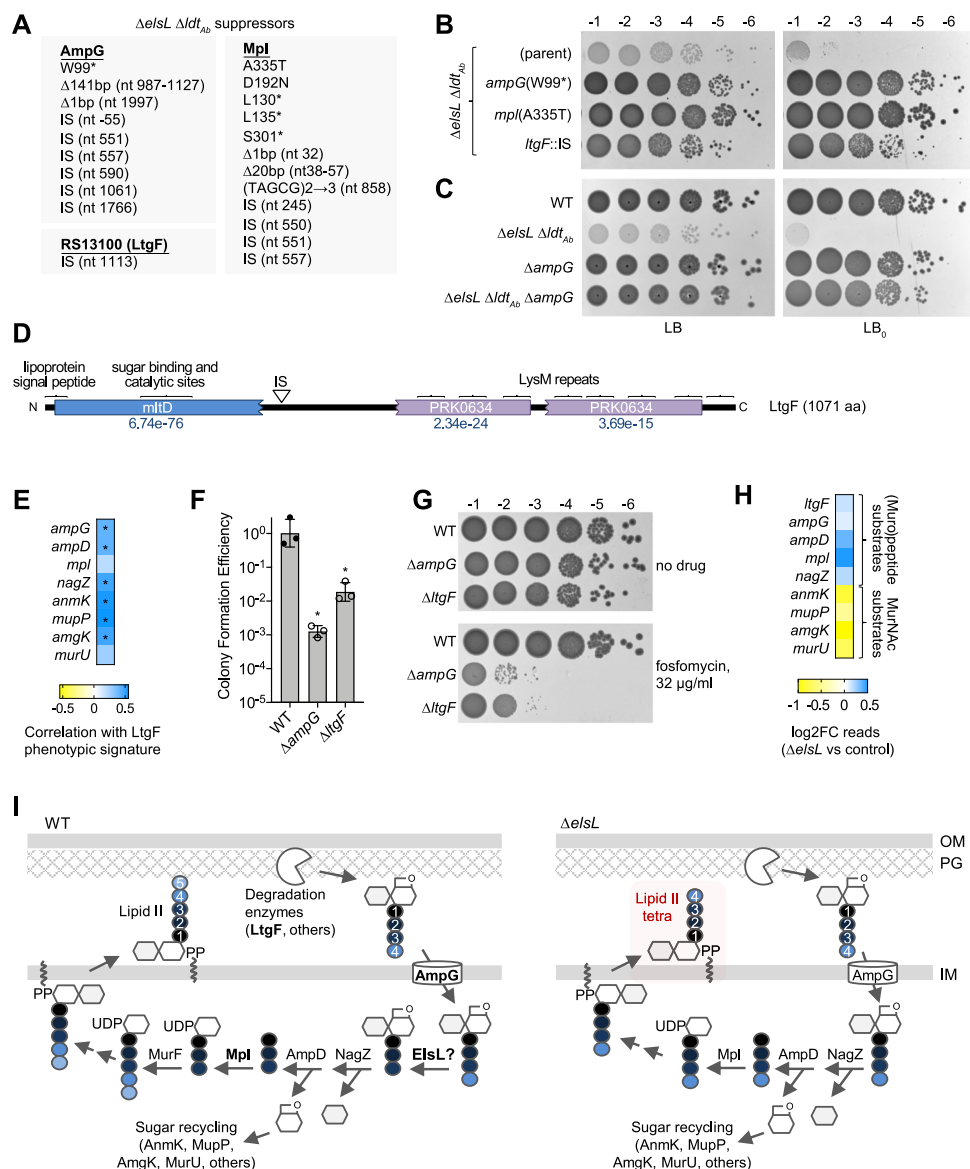
FIG 5 Blocking early cell wall-recycling proteins or the Mpl peptide-recycling ligase suppresses ΔelsL Δldt_Ab synthetic lethality. (A) Listed are mutations identified by whole-genome sequencing in derivatives of ΔelsL Δldt_Ab allowing enhanced colony formation on LB or LB_0 agar medium. The protein effect is listed in the case of substitutions; in all other cases, the mutation and the corresponding nucleotide (nt) position relative to the gene start are listed. IS, insertion sequence. (B and C) The indicated spontaneous mutant and the ΔelsL Δldt_Ab parent strain (B), or the indicated deletion mutants and WT control (C) were serially diluted and spotted on LB (left) or LB_0 (right) agar medium, and the resulting colonies were imaged as in Fig. 3. (D) Schematic of LtgF protein. IS indicates the location affected by the ISAba1 suppressor mutation in ltgF. Rectangles and brackets indicate predicted domains from CDD or SignalP. CDD E values are listed; E values of the LysM domains were below 1e-5. (E) LtgF and canonical cell wall-recycling genes have correlated phenotypic signatures. The heat map shows the Pearson correlation coefficient (r) measuring relatedness of the Tn-seq phenotypic signatures (5) of each gene with that of ltgF. *, P < 0.05. (F and G). The susceptibility to fosfomycin (32 μg/mL) was determined by CFE assay. Bars (F) show the geometric mean ± SD (n = 3 biological replicates). *, P < 0.0001 in unpaired t tests comparing each mutant to the WT. Representative colonies are shown in G. (H) Direction of the Tn-seq genetic interaction between elsL and cell wall-recycling genes depends on the component being recycled. The heat map shows the fold change in Tn-seq read counts of the indicated gene in the ΔelsL mariner library versus that in the WT control library (Data Set S1). (I) Model for the role of ElsL in A. baumannii cell wall recycling. (Left) PG is degraded by lytic transglycosylases (e.g., LtgF) and endopeptidases to release anhydro-MurNAc-containing products. Anhydro-MurNAc-tetrapeptides imported by AmpG are processed to tripeptide form by ElsL. After removal of the PG amino sugars, the tripeptide is reused via ligation to UDP-MurNAc by Mpl, followed by addition of D-Ala-D-Ala to result in UDP-MurNAc-pentapeptide and ultimately lipid II. In the absence of ElsL, in contrast, tetrapeptides are reused by Mpl, resulting in synthesis of aberrant lipid II tetrapeptide (right).
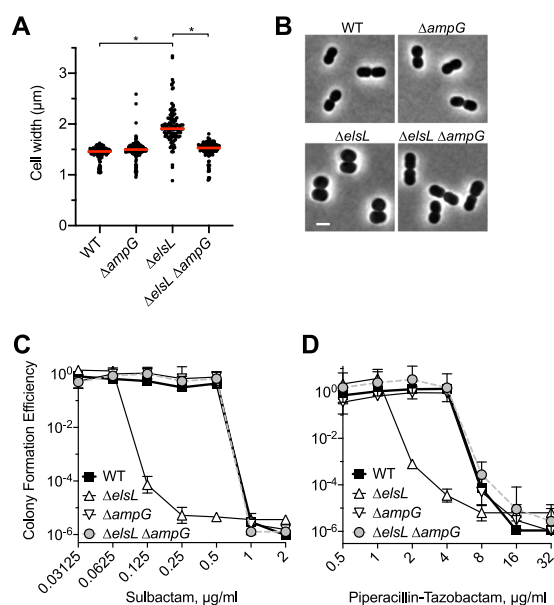
FIG 6 Blocking cell wall recycling suppresses morphology and antibiotic hypersusceptibility defects of the ΔelsL mutant. (A and B) ampG deletion restores the rod shape in the ΔelsL strain. Cells were imaged by phase-contrast microscopy, and cell width was measured by image analysis (A). Lines show median values ($n \geq 102$). *, $P < 0.0001$ in the Kruskal-Wallis test. Representative cells are shown in panel B. Scale bar, 2 μm. (C and D) ampG deletion reverses ΔelsL hypersusceptibility to divisome-targeting β-lactams. Susceptibility to sulbactam (C) and piperacillin-tazobactam (D) was measured by CFE assay. Data points show the geometric mean ± SD ($n = 3$ biological replicates).

tetrapeptide and, ultimately, incorporation of tetrapeptide stems into the cell wall (Fig. 5I, right). These stems are toxic dead-ends, as they cannot be used as donors in cross-link formation by PBPs (39). This would account for the decrease in overall cross-links seen with ΔelsL (Fig. 1E and H). Toxicity would be limited to some extent by Ldt_{Ab}, since LDTs use tetrapeptides as donors (6); this would account for the elevated level of L,D-cross-links seen with ΔelsL (Fig. 1F). Absent Ldt_{Ab}, however, the uncrosslinked tetrapeptide stems would compromise cell wall integrity, accounting for the aggravated phenotypes (Fig. 4). Preventing tetrapeptide reuse by suppressor mutations would efficiently bypass this toxic pathway.

Block in cell wall recycling suppresses ΔelsL shape and susceptibility defects. We interrogated the ElsL LDC model through parallel genetic and biochemical approaches. First, given the ability of muropeptide recycling block to enhance ΔelsL Tn-seq fitness (Fig. 5H), we tested the degree to which such a block also alleviates ΔelsL morphological and antibiotic hypersusceptibility phenotypes. Blocking cell wall recycling by ampG mutation completely restored a short rod shape to cells lacking ElsL, with median cell width returning to the WT value (Fig. 6A and B). ΔelsL bacteria are hypersusceptible to antibiotics that attack division septum PG synthesis, such as sulbactam (5). ampG deletion also completely reversed this defect. While ΔelsL was unable to form colonies on solid medium with low doses of sulbactam, ΔelsL ΔampG grew efficiently, restoring the MIC to a WT level (1 μg/mL; Fig. 6C). This effect extended to another treatment predicted to target septal PG synthesis, the broad-spectrum combination drug piperacillin-tazobactam (40). Specific block of divisional PG synthesis by piperacillin-tazobactam was supported by the dramatic elongation of WT cells in the presence of the drug at levels at or below the MIC (Fig. S5A) and by the marked hypersusceptibility of an elongation-defective Rod system mutant, Δpbp2 (Fig. S5B). ΔelsL similarly showed increased susceptibility to piperacillin-tazobactam, which was reversed by reintroducing the WT allele (Fig. S5B and C). Unlike the WT, ΔelsL did not form elongated filaments in the presence of piperacillin-tazobactam but instead grew as enlarged spheroids (Fig. S5A), similar to genetic interaction results (Fig. S3A) and consistent with the notion that elsL mutation impairs cell
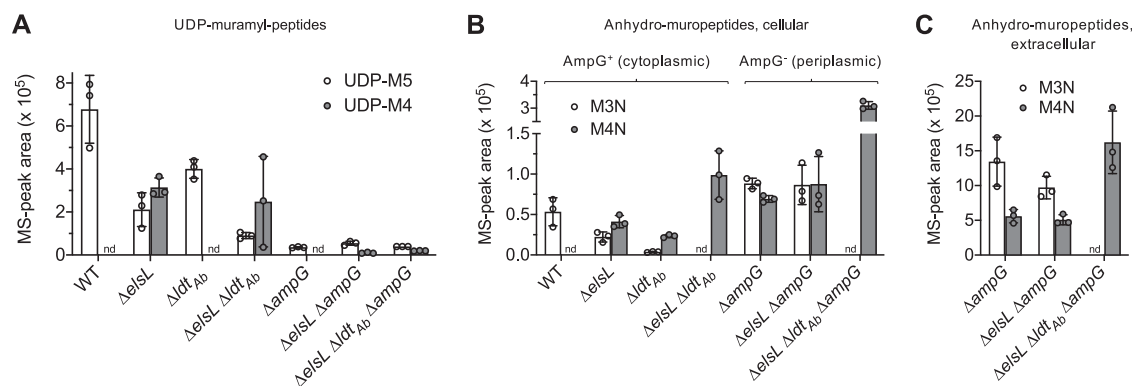
FIG 7 ElsL absence causes accumulation of cytoplasmic tetrapeptide recycling intermediates and a reduction in pentapeptide precursor synthesis that is bypassed by *ampG* deletion. (A) UDP-muramyl-peptides (UDP-M5, UDP-M4) were detected by MS in the cellular fraction from cultures of the indicated strains. (B and C) Anhydro-muropeptides (M3N and M4N) were detected in the intracellular (B) and extracellular (supernatant, C) fractions by MS from cultures of the indicated strains. In panel B, anhydro-muropeptides detected in AmpG⁺ cultures are imported and thus reflect cytoplasmic levels; detection of these PG turnover products in AmpG⁻ cultures, in which they are not efficiently imported, thus reflects levels in the periplasm. Bars show the mean ± SD (*n* = 3 biological replicates). nd, not detected.

wall elongation. Notably, hypersusceptibility of Δ*elsL* to piperacillin-tazobactam was also fully reversed by removing cell wall recycling through deletion of *ampG* (Fig. 6D). Together, these results are consistent with ElsL deficiency owing its multiple toxic phenotypes to recycling of aberrant cell wall intermediates.

ElsL deficiency causes accumulation of aberrant cytosolic tetrapeptides and disrupts the synthesis of pentapeptide precursors. We further tested the potential recycling LDC function of ElsL by measuring its effect on levels of PG precursors *in vivo*. Canonical recycling LDCs act on tetrapeptide-containing products derived from turnover of the cell wall (6, 7). The resulting tripeptides lead to generation of the key cytosolic building block UDP-MurNAc pentapeptide (UDP-M5) (Fig. 5I, left); aberrant reuse of unprocessed tetrapeptides, in contrast, would lead to the potentially toxic UDP-MurNAc tetrapeptide (UDP-M4) (Fig. 5I, right). UDP-M4 should therefore show higher levels in ElsL⁻ versus ElsL⁺ *A. baumannii* if the protein functions as an LDC. To test this prediction, we analyzed UDP-linked muramyl-peptides within the bacterial strains via UPLC-MS. In contrast to ElsL⁺ strains, which had UDP-M5 without detectable UDP-M4 (Fig. 7A, WT and Δ*ldt*Ab), ElsL⁻ mutants showed abundant UDP-M4 with a concomitant decrease in UDP-M5 (Fig. 7A, Δ*elsL* and Δ*elsL* Δ*ldt*Ab), consistent with tetrapeptide substrate buildup due to an absence of LDC function. Analysis of isogenic AmpG⁻ strains revealed the likely mechanism of suppression of blocking cell wall recycling. Compared to AmpG⁺, AmpG⁻ variants showed dramatically reduced amounts of UDP-M4 that were now below the level of UDP-M5 (from *de novo* biosynthesis) in each strain (Fig. 7A, Δ*elsL* Δ*ampG* and Δ*elsL* Δ*ldt*Ab Δ*ampG*). AmpG deletion therefore prevents the toxic tetrapeptide products from being reused for PG synthesis, explaining how recycling mutations bypass the toxic phenotypes of ElsL deficiency.

Examination of anhydromuropeptides, the turnover-derived fragments that are recycled into UDP-linked precursors, further supports the critical function of ElsL as a recycling LDC. In the WT, anhydromurotripeptide (M3N) but not anhydromurotetrapeptide (M4N) was detected in the cellular fraction (Fig. 7B). In contrast, Δ*elsL* had a buildup of M4N (Fig. 7B), consistent with lack of a recycling LDC. The AmpG permease is required for cytosolic import of anhydromuropeptides (35); detection of these products in AmpG⁻ cultures thus reflects a periplasmic or extracellular, rather than cytoplasmic, locale. In contrast to the results with AmpG⁺ strains, *elsL* deletion did not affect periplasmic (Fig. 7B) or extracellular (Fig. 7C) levels of M4N in the Δ*ampG* background (compare Δ*elsL* Δ*ampG* to Δ*ampG*). These results are consistent with ElsL providing only a cytoplasmic LDC function. We note that some M3N was detected in Δ*elsL*, despite the strain lacking the putative recycling LDC; in addition, an M4N increase and M3N decrease (versus WT) was observed with Δ*ldt*Ab, despite the presence of the

putative LDC (Fig. 7B). In each of these cases, the levels of these anhydromuropeptides can be explained as reflecting the compositionally altered cell walls from which they derive (e.g., the Δldt_{Ab} wall lacks tripeptide stems, while $\Delta elsL$ accumulates them; Fig. 1E). In the case of $\Delta elsL$ Δldt_{Ab}, the large increase in M4N and undetectable M3N (Fig. 7B and C) are consistent with the combined effect of no cytosolic LDC activity and altered cell wall composition.

ElsL has LDC activity paralleling that of *E. coli* LdcA. Three additional results support the model that ElsL is the missing LDC in *A. baumannii*. First, $\Delta elsL$ defects are reversed by LdcA, the canonical LDC from *E. coli*. To show this, each protein was 3×-FLAG-tagged and expressed in $\Delta elsL$ under IPTG control, and IPTG concentrations yielding equivalent protein levels were determined (50 μM with ElsL$_{FLAG}$; 500 μM with LdcA$_{FLAG}$; Fig. 8A; Fig. S2B). Using these conditions, both enzymes completely reversed the sulbactam hypersusceptibility of $\Delta elsL$ (Fig. 8B). At lower expression levels, LdcA caused partial complementation, while full complementation was still seen with ElsL (Fig. 8A and B; compare $ldcA_{FLAG}$ 50 with $elsL_{FLAG}$ 0 μM IPTG [leaky expression]). These results confirm that the $\Delta elsL$ defect is due to deficient LDC activity and suggest that *A. baumannii* cell wall recycling has evolved to be most efficient with the ElsL YkuD-family LDC.

Second, ElsL activity depends on a cysteine residue that aligns with the conserved catalytic cysteine of YkuD-family LDTs (41, 42). ElsL harboring a mutation at this site (C138S) lost all ability to confer intrinsic sulbactam resistance to $\Delta elsL$ when expressed in *trans* (Fig. 8D), despite high-level induction with 500 μM IPTG (Fig. 8C; Fig. S2C).

Third, purified ElsL has LDC activity *in vitro*. ElsL and *E. coli* LdcA, a positive control for LDC activity, were both purified using a C-terminal His tag and assayed in parallel. LDCs cleave between the D-alanine and the meso-diaminopimelic acid only in disaccharide tetrapeptides (M4) and not in disaccharide pentapeptides (M5); we thus used these two muropeptides to assay LDC activity. Similar to LdcA, ElsL completely cleaved the M4 substrate to the disaccharide tripeptide (M3) (Fig. 8E and F). ElsL had no activity on M5 (Fig. 8E and F). ElsL thus possesses selective LDC activity. We conclude that ElsL is a novel type of cell wall-recycling enzyme using a cytoplasmic YkuD-family domain to catalyze the key LDC reaction.

The ElsL LDC family includes orthologs in diverse bacteria. Search of a database of ~14,000 representative bacterial genomes (Materials and Methods) revealed predicted cytoplasmic ElsL orthologs in a range of different organisms (Data Set S3). Orthologs were found mainly within the *Proteobacteria*, with the largest representation by diverse members of the *Gamma*- and *Betaproteobacteria* classes (624 and 101, respectively, out of 788 total hits identified). This included the intracellular pathogens *Legionella pneumophila* and *Coxiella burnetii* (43). A total of 5/21 gammaproteobacterial and 2/6 betaproteobacterial orders did not contain ElsL orthologs, suggesting that while relatively widespread, the enzyme may have been lost or replaced by other LDCs in those cases. ElsL orthologs were also present in all orders of the *Verrucomicrobia*, including the human gut microbiota member *Akkermansia muciniphila*. In sum, a large number of diverse bacterial species appear to have evolved to use the cytoplasmic ElsL-class LDC for recycling of the cell wall.

DISCUSSION

We report here the identification of a novel class of cytoplasmic LDC that enables cell wall recycling in *A. baumannii*. This class uses a cysteine-containing catalytic domain usually found in LDT proteins. ElsL is the founding member of this family, and orthologs were identified in a range of other bacteria. ElsL deficiency causes a number of phenotypes: (i) loss of rod shape, (ii) impaired growth, (iii) hypersensitivity to septal cell wall-targeting antibiotics, and (iv) cell wall structural defects, including increased 3-3 cross-links with reduced overall cross-linkage. Most of these phenotypes are aggravated by mutating the enzyme necessary for 3-3 cross-link formation (Ldt$_{Ab}$) or by low osmolarity, while they are suppressed by blocking muropeptide recycling. Each of these features is explained by the model that ElsL is the LDC that processes turnover-derived muropeptides in *A. baumannii*, with toxic $\Delta elsL$ phenotypes caused by the
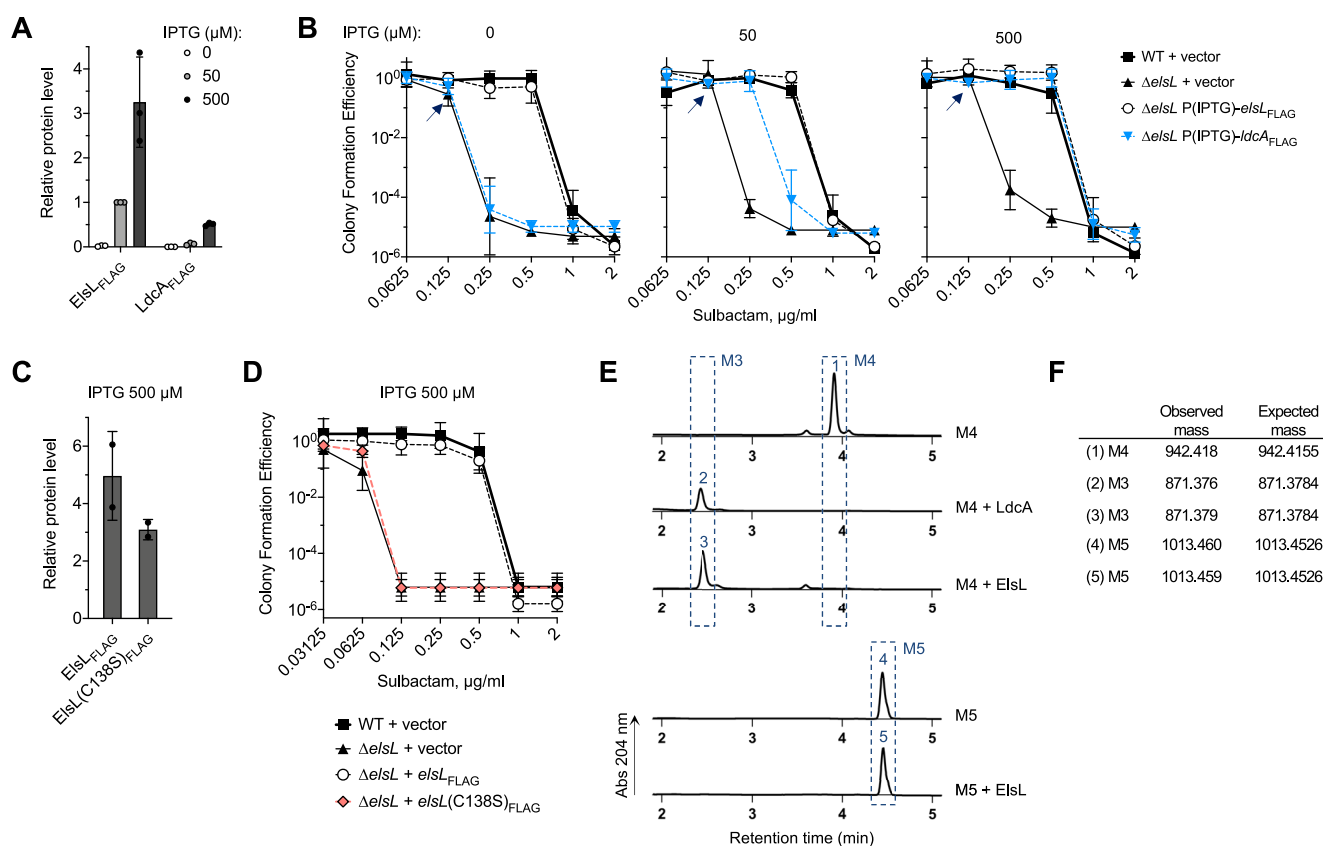
FIG 8 ElsL is the missing-link PG recycling L,D-carboxypeptidase in *A. baumannii*. (A) Western blot quantification of ElsL_FLAG and LdcA_FLAG. Δ*elsL* bacteria with inducible expression of each enzyme by P(IPTG) were cultured with the indicated IPTG concentration. Data points show protein level (relative to ElsL_FLAG, IPTG 50 μM) determined from image analysis. Bars show the mean ± SD (*n* = 3 biological replicates). (B) *E. coli* LdcA reverses the Δ*elsL* sulbactam hypersusceptibility defect. Susceptibility was determined by CFE assay. Plates contained the indicated sulbactam and IPTG concentrations. Data points show the geometric mean ± SD (*n* = 3 biological replicates). Arrows denote that colonies formed by Δ*elsL* + vector on 0.125 μg/mL sulbactam medium were pinpoint-sized. (C) Western blot quantification of ElsL_FLAG in Δ*elsL* bacteria with the indicated P(IPTG)-inducible allele cultured in the presence of 500 μM IPTG. Data points show the protein level (relative to ElsL_FLAG, IPTG 50 μM) as in panel A, except *n* = 2. (D) Intrinsic sulbactam resistance conferred by ElsL depends on an active site cysteine. Susceptibility to sulbactam was determined by CFE as in panel B. (E and F) ElsL has LDC activity *in vitro*. Shown are UPLC chromatograms of the reaction products following incubation of substrate (M4, murotetrapeptide, top; or M5, muropentapeptide, bottom) with the indicated purified enzyme (E). Numbered peaks were identified based on retention time and confirmed by MS (F). Minor peaks, which were trace muropeptide contaminants arising during manual HPLC purification of M4 and M5 substrates from *C. crescentus* PG (Materials and Methods), were identified as M5^Gly (at minute ~3.6) and M2 (at minute ~4.1).

deleterious tetrapeptides that accumulate absent this processing. Analysis of cell wall precursors supported this model and showed that tetrapeptide-containing biosynthetic intermediates increase in Δ*elsL* bacteria at the expense of the mature pentapeptide building blocks (Fig. 7). When incorporated as part of nascent cell wall, these tetrapeptides cannot be used as donors in 4-3 bond formation by PBPs and thus diminish overall cell wall cross-linkage (Fig. 1H). Periplasmic LDTs, however, can act on tetrapeptides, likely mitigating their toxic effects and explaining the synthetic lethality of the double *elsL ldt_Ab* mutant (Fig. 4). ElsL has LDC activity *in vitro*, catalyzing the removal of the terminal D-Ala from disaccharide tetrapeptides but not pentapeptides (Fig. 8E), solidifying its critical role in muropeptide recycling.

The highly similar phenotypes resulting from loss of ElsL and loss of Rod system proteins suggest a possible relationship between recycling LDC activity and the ability of cell wall elongation to proceed normally in *A. baumannii*, although the exact basis for the linked phenotypes remains to be elucidated. The shared phenotypes include loss of rod morphology as well as highly correlated antibiotic susceptibility signatures defined by marked hypersensitivity to division-targeting β-lactams (Fig. S5B) (5). In addition, the Δ*elsL* growth defect was aggravated by mutation of nonessential cell division genes (Fig. 3), which mirrors the effect of antibiotics blocking division (Fig. 6). Further, Δ*elsL* was

unable to form elongated filaments under conditions of impaired division (Fig. S3A and S5A). Together, these results are consistent with the model that the Rod system is defective when cells lack ElsL, resulting in a heavy reliance on divisome PG synthesis and hypersusceptibility to inhibition of this process. Given its diffuse cytoplasmic location, the recycling LDC is almost certainly not a requisite component of the Rod complex. An alternative possibility is that accumulation of tetrapeptide intermediates is directly or indirectly responsible for Rod system failure. That aberrant intermediates may have selective effects on a particular PG biosynthetic machine is supported by previous work with *E. coli* showing that PG precursor composition can determine a cell's preference for lateral versus septal cell wall growth (44–46). For instance, increasing the levels of a D,D-carboxypeptidase, which cleaves the terminal D-alanine on pentapeptide subunits to yield tetrapeptides, caused rod-shaped WT cells to grow as spheres (45) and allowed filamentous *pbp3* hypomorphs to shorten and divide more efficiently (44). These findings are consistent with the model that the Rod system prefers to act on PG with pentapeptide subunits and does not use tetrapeptides (or their tripeptide derivatives) efficiently (44, 45). The opposite may be true of the divisome, in which the main transpeptidase, PBP3, is thought to prefer or require tripeptides, originating from tetrapeptides, as the acceptor muropeptide (47, 48). Interestingly, dramatic Rod⁻ phenotypes are also seen with mutation of *A. baumannii dacC* (5), a predicted PG hydrolase that may also modulate the balance of cell wall peptide substrates in ways promoting lateral cell wall growth. The idea that cell wall subunit levels determine Rod system versus divisome activity may also contribute to the mitigation of toxicity in Δ*elsL* cells by Ldt$_{Ab}$, in agreement with what was proposed in reference 6. While this mitigation is likely due to provision of alternative, supportive cross-links, an additional possibility is that Ldt$_{Ab}$ directly or indirectly generates tripeptide substrates in Δ*elsL* that are needed for optimal cell division. Further work is required to understand the mechanisms by which alterations to cell wall stem peptides in *A. baumannii* drives the function (and malfunction) of specific PG biosynthesis enzymes.

Our genetic interaction analysis revealed an additional interdependent relationship between ElsL and the Mla lipid transport pathway. The Mla proteins mediate retrograde transport of phospholipids from the OM to the inner membrane, facilitating lipid asymmetry in the OM (25, 49). The system may also prevent excessive loss of lipids in the form of OM vesicles (OMVs) (50, 51). Interestingly, an *elsL* mutant sheds larger amounts of OMVs than the WT (8). It is thus possible that membrane lipid loss contributes to the aggravating phenotype of the *elsL mla* double mutant. Another possibility is that combining an impaired cell wall (due to low cross-linkage, ElsL⁻) with a compromised OM (Mla⁻) leads to synergistic failure of envelope mechanical integrity (52), manifesting as an aggravated growth defect. In sum, a variety of pathways, including those determining alternative cross-link formation, cell division, and OM homeostasis, become indispensable in the absence of ElsL function, underlining the importance of this key enzyme to multiple facets of *A. baumannii* envelope biogenesis.

The novel ElsL class of cell wall-recycling LDC identified in this work uses a cysteine catalytic residue, contrasting it from that of the two described recycling LDC enzymes, LdcA and LdcV. LdcA, found in *E. coli*, *Pseudomonas aeruginosa*, and several other organisms, is a serine peptidase that uses a Ser-His-Glu catalytic triad (53), while LdcV, identified recently in *Vibrio cholerae*, *Aeromonas hydrophila* and *Proteus mirabilis*, belongs to the LAS superfamily of zinc-dependent metalloproteases that use an active site zinc ion coordinated by histidines (6, 54). While all three LDC classes enable muropeptide recycling, they may differ in their relative preferences for the variety of potential tetrapeptide-containing substrates derived from the cell wall (7), although this remains to be determined. The identification of a distinct, noncanonical class of LDC related to LDTs has two important implications. First, the finding helps illuminate the muropeptide recycling pathway in many bacteria, such as *A. baumannii*, that lack a homolog of the previously identified recycling LDCs (35). Lack of a known LDC homolog in such bacteria has been explained previously by the possibility that they bypass the need for a recycling LDC due to low cell wall tetrapeptide content or high Mpl selectivity against tetrapeptides (35). While these

mechanisms may be true in many cases, an alternative explanation is that a range of organisms possess a nonclassical LDC (e.g., of the ElsL family), allowing the typical peptide recycling loop to be fully closed. Second, the reliance of *A. baumannii* on two YkuD-domain proteins for maintaining the cell wall points to a unique potential vulnerability in this highly resistant pathogen. Simultaneously targeting the catalytic cysteines in both ElsL and Ldt_{Ab} could exploit the synthetic lethality of the two proteins to potently weaken the sacculus of the pathogen and inhibit growth. Copper (14) and carbapenem antibiotics (55), known inhibitors of LDT proteins, are candidates for such a strategy.

In conclusion, we have identified a new family of LDC critical to muropeptide recycling in *A. baumannii* and likely many other organisms. Our combined genetic and biochemical interrogation of ElsL function provided insights into the role of the protein in recycling as well as its pleiotropic influence on numerous pathways important to envelope integrity and growth. Future work will examine the mechanisms by which changes to cell wall precursors in cells showing altered expression of ElsL or other muropeptide-modifying enzymes lead to preferential action/inaction of specific PG synthesis machines, which will likely shed light on how cell wall synthesis and cell proliferation are coordinated in *A. baumannii*. Furthermore, the vulnerabilities exposed by ElsL inhibition, precursor buildup, and their network of toxic effects present opportunities for the rational development of improved antimicrobials aimed at controlling this intractable pathogen.

MATERIALS AND METHODS

Bacterial strains and growth conditions. The bacterial strains used in this work are described in Table S2. *A. baumannii* strains were derivatives of ATCC 17978. Bacteria were cultured in lysogeny broth (10 g/L tryptone, 5 g/L yeast extract, 10 g/L NaCl) (LB), unless otherwise noted. Liquid cultures were incubated at 37°C in flasks with orbital shaking or in tubes with rotation via roller drum. Growth was monitored by measuring absorbance at 600 nm. LB agar was supplemented with antibiotics (carbenicillin [Cb] at 25 to 100 μg/mL, kanamycin [Km] at 10 to 20 μg/mL, gentamicin [Gm] at 10 μg/mL) or sucrose (10%) as needed (Sigma-Aldrich). LB prepared without NaCl (LB₀) was used in phenotypic testing where noted. Superoptimal broth with catabolite repression (SOC) was used in Tn-seq library preparation, and Vogel Bonner medium (VBM) supplemented with Gm (10 μg/mL) was used for isolation of CRISPRi strains containing miniTn7 constructs.

Molecular cloning and strain construction. The plasmids used in this study are listed in Table S2. Most DNA constructs were generated by PCR-amplification using oligonucleotide primers (Integrated DNA Technologies [IDT]; Table S2) and cloning in the HincII site of pUC18, followed by verification by sequencing (Genewiz) before subcloning in subsequent vectors. Plasmids for complementation, localization, allele exchange, and sgRNA production were introduced into *A. baumannii* ATCC 17978 by electroporation (56).

(i) Complementation and localization experiments. To generate an ldt_{Ab} plasmid for HADA experiments, the EcoRI and PstI fragment from pYDE231 was subcloned downstream of the T5lacP promoter in pEGE305 to generate pYDE240. To construct *elsL*- and *ldcA*-3xFLAG fusions for complementation experiments, the BamHI-XbaI fragment from pYDE342 and pYDE343 were each subcloned in pJE42, which provides an in-frame C-terminal 3×FLAG sequence, generating pYDE346 and pYDE347. The hybrid genes were then subcloned into pEGE305 using EcoRI and PstI, resulting in pYDE350 ($ElsL_{FLAG}$) and pYDE351 ($LdcA_{FLAG}$). To construct *msGFP2* gene fusions, a codon-optimized *msGFP2* reporter gene containing an in-frame polyglycine linker was first synthesized as a double-stranded DNA fragment by IDT and cloned in the HincII site of pUC18 (pAFE225). The BamHI-XbaI fragments from pYDE342 and pYDE063 were cloned in pAFE225, generating pYDE386 (*elsL-msGFP2*) and pYDE387 (ldt_{Ab}-*msGFP2*). The gene fusions were then cloned into pEGE305 using EcoRI and PstI, generating pYDE389 and pYDE390, respectively. To generate an independent *msGFP2* control gene, *msGFP2* was amplified from pAFE225 using a primer (msGFP2_F) that replaces the XbaI site and glycine linker with EcoRI, ribosome binding, and translational start sites. The PCR product was then directly cloned into pEGE305 using EcoRI and PstI sites, generating pAFE256. An $elsL_{FLAG}$(C138S) mutant was constructed by replacing the EcoRI-BstBI fragment of pYDE350 with a fragment amplified with a primer (elsL-C138S-R) containing the substitution mutation.

(ii) Overexpression and purification of *elsL* and *ldcA*. The NcoI-EcoRI fragments from pYDE281 and pYDE324, respectively, were each cloned upstream of the in-frame 6×His tag sequence in pET28b, creating (pYDE290 and pYDE328).

(iii) Gene deletions. Deletion mutants were isolated using homologous recombination/allelic exchange using sucrose counterselection as described (57). A $\Delta elsL$ Δldt_{Ab} double mutant (EGA740) was constructed by allelic exchange with pEGE268 in EGA739 (5); the strain was isolated as small, sucrose-resistant colonies after overnight 30°C incubation followed by 1 day at room temperature. A $\Delta elsL$ $\Delta ampG$ double mutant (YDA411) was isolated by allelic exchange with pEGE268 in EGA516 (58). A $\Delta elsL$ Δldt_{Ab} $\Delta ampG$ triple mutant (YDA414) was isolated by allelic exchange with pEGE271 in YDA411. In-frame deletion of *ltgF* was constructed by three-way ligation of ~1 kb flanking homology arms with pJB4648.

(iv) CRISPRi. sgRNAs were constructed by PCR-amplifying 24-base, protospacer-adjacent motif (PAM)-adjacent target regions satisfying previously described criteria (59, 60), followed by cloning directly into the SpeI and ApaI sites of pYDE007 (27) and verification by restriction digestion and sequencing. $\Delta elsL$ and

Δldt_{Ab} strains with inducible *dcas9* were isolated by introducing pYDE009 (27) into EGA738 and EGA739 via four-parental mating (57, 61); transposants were isolated on VBM-Gm10 plates, generating YDA186 and YDA095, respectively. Integration at the *attTn7* locus was confirmed by PCR, and loss of pYDE009 was confirmed by screening on Cb plates (62, 63).

Construction of transposon mutant libraries. Mutagenesis of $\Delta elsL$ (EGA738) and Δldt_{Ab} (EGA739) with the *mariner* transposon was performed by electroporation with pDL1100 (5). Cells were then diluted with 1 mL SOC, allowed to incubate for 15 min at 37°C, and spread on membrane filters (0.45-μm pore size) overlaid on prewarmed SOC agar plates. Plates were incubated at 37°C for 1 h, and filters were transferred to solid LB supplemented with Km (10 μg/mL with $\Delta elsL$ and 20 μg/mL with Δldt_{Ab}). After overnight incubation at 37°C, colonies were lifted from filters by agitation in sterile phosphate-buffered saline (PBS), mixed with sterile glycerol (10%), aliquoted, and stored at -80°C. Approximately 160,000 mutant colonies from 19 subpools were analyzed in the $\Delta elsL$ strain, and approximately 300,000 from 20 subpools were analyzed with the Δldt_{Ab} strain.

Tn-seq library amplification, sequencing, and analysis. Genomic DNA was extracted from samples using the DNeasy kit (Qiagen) and quantified using a SYBR green I (Invitrogen) microplate assay. Transposon-adjacent DNA was tagmented and amplified for Illumina sequencing as described (5, 64). Samples were multiplexed, reconditioned, and size selected (250 or 275 to 600 bp; Pippin HT) before sequencing (single-end 50 bp) using primer mar512 on a HiSeq 2500 instrument with high output V4 chemistry at the Tufts University Genomics Core Facility (TUCF-Genomics).

Sequencing reads were quality-filtered, clipped of adapters, and mapped to the *A. baumannii* chromosome (GenBank accession no. NZ_CP012004) with Bowtie (27). Mapped reads were tabulated in wig format according to the position of their TA sites in the NZ_CP012004 genome using custom python scripts (27). To examine genetic interactions between transposon mutations and the deleted gene, data sets were analyzed using the resampling method in the TRANSIT software package (parameters: samples=10000000, norm=TTR, histograms=False, adaptive=True, excludeZeros=False, pseudocounts=0.0, LOESS=False, trim_Nterm=0.0, trim_Cterm=10.0) (65), using previously published WT *mariner* libraries as the control data set (27). Resampling P values were adjusted for multiple comparisons (q value) using the method of Benjamini and Hochberg. Results were visualized as volcano plots using Prism 8. Genes having a low mean read count (<5) in both the deletion and control data sets (essential genes) were not plotted. Hits were defined as genes having a q value of <0.05, ≥ 3 transposon sites, and >5 mean read counts in both data sets. To visualize Tn-seq read counts along chromosomal regions, TTR-normalized counts were merged into a single wig file, scaled such that median read coverage at nonzero insertion sites was equivalent between data sets, and viewed using Integrative Genomics Viewer (27, 66).

Microscopy. Bacteria in the log phase of growth were immobilized on agarose pads (1% in PBS) prior to imaging. For HADA labeling experiments, bacteria were pulsed with 1 mM HADA (Tocris Bioscience) for 15 min, fixed with 70% ice-cold ethanol for 10 to 15 min, and washed twice with PBS before imaging. For localization experiments, strains harboring IPTG-inducible gene fusions to msGFP2 were cultured with 100 μM IPTG prior to imaging. Micrographs were acquired with a 100×/1.4 phase-contrast objective on a Zeiss Axio Observer 7 microscope. A Colibri 7 LED light source was used for fluorescence illumination. Imaging of GFP fluorescence used the 475-nm LED and filter set 92 HE. Imaging of HADA fluorescence used the 385-nm LED and filter set 96 HE. For analysis of HADA incorporation, Fiji software (67) was used for background subtraction from the HADA signal and for determining cell boundaries from stacked HADA and phase images. Fluorescence intensity across populations of cells in multiple fields was then plotted as demographs using MicrobeJ software (68). For analysis of cell width, the maximal width relative to the medial axis of each cell was quantified from phase images using MicrobeJ (68).

Genetic interaction and antibiotic susceptibility tests. Bacteria (optical density [OD], 1) were serially diluted 10-fold in PBS and spot-plated on the noted solid medium. After overnight growth at 37°C, colonies were imaged with transilluminated light on a ChemiDoc MP imaging system (Bio-Rad). For genetic interaction analysis, colony diameters were measured using ImageJ (69) and normalized to the WT control (YDA007). Genetic interactions were analyzed by comparing the relative colony diameter values of strains harboring two genetic lesions (CRISPRi knockdown of candidate gene and deletion of $\Delta elsL$) with the hypothetical values expected from a multiplicative model, in which the values of each single-lesion strain are multiplied (70). Sensitivity to sulbactam and to piperacillin-tazobactam (8:1 ratio by mass) was measured with a colony formation efficiency (CFE) assay (58). Serial dilutions of WT and isogenic mutant strains were spotted on solid LB agar medium containing graded concentrations of drug (or no drug control). After overnight growth at 37°C, colony counts were determined and compared to the no-drug control. The limit of detection was approximately 10^{-5} to 10^{-6}.

PG isolation and analysis. Sacculi isolation and PG analysis were performed as previously described (71). In short, *A. baumannii* cells from overnight LB cultures were harvested, resuspended in LB + 5% SDS, and boiled with stirring for 2 h followed by stirring at room temperature overnight. SDS was removed from sacculi through several rounds of ultracentrifugation and resuspension with MilliQ water. Sacculi were then resuspended in 100 mM Tris-HCl pH 8.0 buffer with proteinase K (20 μg/mL) and incubated at 37°C for 1 h. The reaction was stopped by adding SDS 1% and boiling at 100°C for 5 min. SDS was removed as described above, and sacculi were resuspended in water. Muramidase was then added, and reaction mixtures were incubated overnight at 37°C to solubilize the sacculi completely. The soluble muropeptides were reduced using $NaBH_4$, and their pH was adjusted before separation using ultraperformance liquid chromatography (UPLC; Waters) and identification using a matrix-assisted laser desorption ionization–time of flight mass spectrometry (MALDI-TOF MS) system (Waters).

For quantification, we chose 2 random PG profiles that were representative of each strain. The area for each identified peak was integrated, giving each individual muropeptide a relative area value based on the

total integrated area. Using these values, the molar percentage was also calculated for each muropeptide. This relative molarity was also used to calculate the degree of cross-linking using the following formula:

$$\text{Degree of crosslinking: } (\text{Rel Mol Dimers}) + (\text{Rel Mol Trimers} \times 2) + (\text{Rel Mol Tetramers} \times 3)$$

Analysis of intracellular and extracellular soluble muropeptides. Bacteria were grown with LB at 37°C for 4 h to log phase, and the OD was recorded. Bacteria were cooled on ice and centrifuged at 25,000 rpm for 20 min at 4°C. Supernatants were stored at 4°C for analysis of extracellular soluble muropeptides, and pellets were used for analysis of the intracellular fraction.

To study PG turnover products and precursors within the intracellular fraction, cell pellets were washed twice with sterile 1% NaCl, resuspended in water, and boiled for 30 min with stirring. Samples were again centrifuged at 25,000 rpm for 15 min, and supernatants were recovered and filtered (0.2-μm pore size). A MALDI-TOF MS system was used for identification of the muropeptides derived from turnover (anhydro species) and synthesis (UDP-activated species). To study muropeptides within the extracellular fraction, supernatants were filtered as described above and immediately boiled for 15 min to precipitate proteins. The soluble fraction was then analyzed using the same MS system as for the intracellular muropeptides, focusing on detection of products derived from turnover that were released into the media. Quantification of all muropeptides used the total-ion count detected by the system. All analyses were performed with biological triplicate samples.

Suppressor mapping by whole-genome sequencing and phenotypic signature analysis. Suppressor mutants bypassing the EGA740 growth defect were isolated on LB or LB_0 plates. Genomic DNA (DNeasy kit) was quantified with a SYBR green I (Invitrogen) microplate assay and used as input for Illumina library preparation using a modified small-volume Nextera tagmentation method as described previously (58). Libraries were sequenced (single-end 100 bp) on a HiSeq 2500 instrument at TUCF-Genomics. Reads were aligned to the NZ_CP012004 genome, and variants were identified using breseq (72). The predicted functional impact of substitution variants was determined by using PROVEAN (73). Identities of ISs were determined by using ISFinder (74). Phenotypic signatures of *ltgF* and cell wall-recycling genes were compared using Qlucore Omics Explorer 3.5, and Pearson correlations were analyzed with Prism 8.

Immunoanalysis of ElsL, Ldt$_{Ab}$, and LdcA proteins. Strains harboring fusion genes or vector control were diluted to OD 0.05 in LB with IPTG (100 μM with msGFP2 fusions; 0, 50, or 500 μM with 3×FLAG fusions) and grown to OD 0.5. Cells were centrifuged and resuspended (50 μL per 1 mL of sample) with SDS sample loading buffer (msGFP2 fusions) or BugBuster protein extraction reagent with 0.1% Lysonase (Millipore) followed by SDS loading buffer (3×FLAG fusions). Samples were boiled for 10 min, separated by SDS-PAGE (12% acrylamide gel), and transferred to an Immobilon-FL polyvinylidene difluoride (PVDF) membrane. Total protein was detected by SYPRO ruby protein blot stain (Invitrogen). GFP was detected by rabbit PABG1 primary (Chromotek; 1:5,000 dilution) and goat anti-rabbit IgG horseradish peroxidase (HRP) secondary (Invitrogen; 1:5,000 dilution) antibodies. FLAG epitope was detected by mouse anti-FLAG M2 primary (Invitrogen; 1:1,000 dilution) and goat anti-mouse IgG HRP secondary (Invitrogen; 1:5,000 dilution) antibodies. Blots were imaged with a ChemiDoc MP system (Bio-Rad). Band intensities were quantified using Image Lab software. Samples were normalized by dividing the immunodetected band intensity by the total protein level from SYPRO staining. Relative values were calculated by dividing each normalized value by the normalized value of the ElsL$_{FLAG}$, 50 μM IPTG sample on the same blot.

Protein overexpression and purification. Overnight cultures of *E. coli* BL21(DE3) strains harboring pYDE290 (*elsL$_{His}$*) or pYDE328 (*ldcA$_{His}$*) were seeded at a 1:100 dilution into 1 L of LB with Km (30 μg/mL) and grown at 37°C to OD 0.6 to 0.8. IPTG was added at 500 μM final, and cultures were incubated at 16°C for 20 h. Cells were harvested, resuspended with 30 mL of prechilled buffer A (50 mM Tris-HCl, 300 mM NaCl), and pulse-sonicated on ice for 15 min. The lysate was clarified by centrifugation at 10,000 × *g* at 4°C for 1 h and filtered (0.45-μm pore size; Millipore). Clarified lysates were loaded on Ni-NTA resin columns (Thermo Scientific) previously equilibrated with 6% (vol/vol) buffer B (50 mM Tris-HCl, 300 mM NaCl, 500 mM imidazole) in buffer A. His-tagged proteins were eluted with gradient concentrations of buffer B (6%, 10%, 30%, 50%, 100%) at 4°C and detected by SDS-PAGE and Coomassie blue staining. Fractions containing the His-tagged proteins were concentrated by using Amicon Ultra-15 centrifugal filter units (10 kDa). Proteins were washed 3 times with 15 mL stocking buffer (50 mM Tris-HCl, 50 NaCl, 10% [wt/vol] glycerol) and resuspended with 200 μL stocking buffer. Proteins were quantified using the Pierce Coomassie Bradford protein assay (Thermo Scientific) and stored as aliquots at −80°C. With ElsL$_{His}$, the elution and stocking buffers included 0.5 mM tris(2-carboxyethyl)phosphine (TCEP) to prevent oxidation of the active-site cysteine residue (75).

***In vitro* assays with ElsL.** LDC activity was assayed *in vitro* using purified proteins and muropeptide substrates. Muropeptide substrates (M4 and M5) were extracted from sacculi isolated from *Caulobacter crescentus*, which are known to have high M4 and M5 content (76), and solubilized as described above. Soluble muropeptides were separated using a high-performance liquid chromatography (Waters) system, and each individual muropeptide was collected manually. Collected fractions were washed from solvents by evaporation using a SpeedVac vacuum concentrator followed by resuspension with MilliQ water. All reactions were performed in 100 mM Tris-HCl, mixing a fraction of M4 or M5 and 10 ng of the corresponding protein (ElsL$_{His}$, LdcA$_{His}$, or none in the negative control). Reaction mixtures were incubated for 2 h at 37°C and stopped by incubation at 100°C for 5 min. After inactivation, the samples were reduced, and their pH was adjusted for injection on the UPLC. Muropeptides were identified according to their retention time, and their identities were validated through MS analysis.

ElsL ortholog identification. *A. baumannii* ElsL (GenBank accession no. WP_000077301) was queried with BLASTp using the refseq_select_prot database, restricting the search to *Bacteria* (representing ~14,000

genomes) and an E value cutoff of 1e-4. From the 1,082 protein sequences that were returned, custom Python scripts were used to identify sequences containing a predicted signal peptide or transmembrane helix (based on the SignalP 5.0 [77], PrediSi [78], Phobius [79], and TMHMM 2.0 [80] methods), or PG-binding domain (from search of the NCBI Conserved Domain Database [CDD] [42]). With SignalP 5.0, an "other" score of <0.75 was used as a conservative marker of potential signal peptides. Hits were excluded if any of the above-mentioned searches were positive. Finally, sequences shorter than 105 or longer than 200 amino acids were excluded. Taxonomic information for the resulting set of ElsL orthologs (788 hits) was obtained from the NCBI database.

Data availability. All sequence data can be found in the NCBI Sequence Read Archive under accession no. PRJNA763919.

SUPPLEMENTAL MATERIAL

Supplemental material is available online only.
DATA SET S1, XLSX file, 0.9 MB.
DATA SET S2, XLSX file, 0.6 MB.
DATA SET S3, XLSX file, 0.1 MB.
FIG S1, PDF file, 0.3 MB.
FIG S2, PDF file, 0.9 MB.
FIG S3, PDF file, 2 MB.
FIG S4, PDF file, 0.5 MB.
FIG S5, PDF file, 1.2 MB.
TABLE S1, PDF file, 0.02 MB.
TABLE S2, PDF file, 0.1 MB.

REFERENCES

1. Sievert DM, Ricks P, Edwards JR, Schneider A, Patel J, Srinivasan A, Kallen A, Limbago B, Fridkin S, National Healthcare Safety Network (NHSN) Team and Participating NHSN Facilities. 2013. Antimicrobial-resistant pathogens associated with healthcare-associated infections: summary of data reported to the National Healthcare Safety Network at the Centers for Disease Control and Prevention, 2009-2010. Infect Control Hosp Epidemiol 34:1–14. https://doi.org/10.1086/668770.

2. Weiner-Lastinger LM, Abner S, Edwards JR, Kallen AJ, Karlsson M, Magill SS, Pollock D, See I, Soe MM, Walters MS, Dudeck MA. 2020. Antimicrobial-resistant pathogens associated with adult healthcare-associated infections: summary of data reported to the National Healthcare Safety Network, 2015-2017. Infect Control Hosp Epidemiol 41:1–18. https://doi.org/10.1017/ice.2019.296.

3. Doi Y, Murray GL, Peleg AY. 2015. Acinetobacter baumannii: evolution of antimicrobial resistance-treatment options. Semin Respir Crit Care Med 36:85–98. https://doi.org/10.1055/s-0034-1398388.

4. Tacconelli E, Carrara E, Savoldi A, Harbarth S, Mendelson M, Monnet DL, Pulcini C, Kahlmeter G, Kluytmans J, Carmeli Y, Ouellette M, Outterson K, Patel J, Cavaleri M, Cox EM, Houchens CR, Grayson ML, Hansen P, Singh N, Theuretzbacher U, Magrini N, WHO Pathogens Priority List Working Group. 2018. Discovery, research, and development of new antibiotics: the WHO priority list of antibiotic-resistant bacteria and tuberculosis. Lancet Infect Dis 18:318–327. https://doi.org/10.1016/S1473-3099(17)30753-3.

5. Geisinger E, Mortman NJ, Dai Y, Cokol M, Syal S, Farinha A, Fisher DG, Tang AY, Lazinski DW, Wood S, Anthony J, van Opijnen T, Isberg RR. 2020. Antibiotic susceptibility signatures identify potential antimicrobial targets in the Acinetobacter baumannii cell envelope. Nat Commun 11:4522. https://doi.org/10.1038/s41467-020-18301-2.

6. Hernandez SB, Dorr T, Waldor MK, Cava F. 2020. Modulation of peptidoglycan synthesis by recycled cell wall tetrapeptides. Cell Rep 31:107578. https://doi.org/10.1016/j.celrep.2020.107578.

7. Templin MF, Ursinus A, Holtje JV. 1999. A defect in cell wall recycling triggers autolysis during the stationary growth phase of Escherichia coli. EMBO J 18:4108–4117. https://doi.org/10.1093/emboj/18.15.4108.

8. Kang KN, Kazi MI, Biboy J, Gray J, Bovermann H, Ausman J, Boutte CC, Vollmer W, Boll JM. 2021. Septal class A penicillin-binding protein activity and LD-transpeptidases mediate selection of colistin-resistant lipooligosaccharide-deficient Acinetobacter baumannii. mBio 12:e02185-20. https://doi.org/10.1128/mBio.02185-20.

9. Aliashkevich A, Cava F. 2021. LD-transpeptidases: the great unknown among the peptidoglycan cross-linkers. FEBS J https://doi.org/10.1111/febs.16066.

10. Hugonnet JE, Mengin-Lecreulx D, Monton A, den Blaauwen T, Carbonnelle E, Veckerle C, Brun YV, van Nieuwenhze M, Bouchier C, Tu K, Rice LB, Arthur M. 2016. Factors essential for L,D-transpeptidase-mediated peptidoglycan cross-linking and beta-lactam resistance in Escherichia coli. Elife 5:e19469. https://doi.org/10.7554/eLife.19469.

11. Mainardi JL, Morel V, Fourgeaud M, Cremniter J, Blanot D, Legrand R, Frehel C, Arthur M, Van Heijenoort J, Gutmann L. 2002. Balance between two transpeptidation mechanisms determines the expression of beta-lactam resistance in Enterococcus faecium. J Biol Chem 277:35801–35807. https://doi.org/10.1074/jbc.M204319200.

12. Hsu YP, Booher G, Egan A, Vollmer W, VanNieuwenhze MS. 2019. d-Amino acid derivatives as in situ probes for visualizing bacterial peptidoglycan biosynthesis. Acc Chem Res 52:2713–2722. https://doi.org/10.1021/acs.accounts.9b00311.

13. Alvarez L, Cordier B, Van Teeffelen S, Cava F. 2020. Analysis of Gram-negative bacteria peptidoglycan by ultra-performance liquid chromatography. Bio Protoc 10:e3780. https://doi.org/10.21769/BioProtoc.3780.

14. Peters K, Pazos M, Edoo Z, Hugonnet JE, Martorana AM, Polissi A, VanNieuwenhze MS, Arthur M, Vollmer W. 2018. Copper inhibits peptidoglycan LD-transpeptidases suppressing beta-lactam resistance due to bypass of

penicillin-binding proteins. Proc Natl Acad Sci U S A 115:10786–10791. https://doi.org/10.1073/pnas.1809285115.

15. Boll JM, Crofts AA, Peters K, Cattoir V, Vollmer W, Davies BW, Trent MS. 2016. A penicillin-binding protein inhibits selection of colistin-resistant, lipooligosaccharide-deficient Acinetobacter baumannii. Proc Natl Acad Sci U S A 113:E6228–E6237. https://doi.org/10.1073/pnas.1611594113.

16. Crepin S, Ottosen EN, Peters K, Smith SN, Himpsl SD, Vollmer W, Mobley HLT. 2018. The lytic transglycosylase MltB connects membrane homeostasis and in vivo fitness of Acinetobacter baumannii. Mol Microbiol 109:745–762. https://doi.org/10.1111/mmi.14000.

17. Le NH, Peters K, Espaillat A, Sheldon JR, Gray J, Di Venanzio G, Lopez J, Djahanschiri B, Mueller EA, Hennon SW, Levin PA, Ebersberger I, Skaar EP, Cava F, Vollmer W, Feldman MF. 2020. Peptidoglycan editing provides immunity to Acinetobacter baumannii during bacterial warfare. Sci Adv 6: eabb5614. https://doi.org/10.1126/sciadv.abb5614.

18. Lonergan ZR, Nairn BL, Wang J, Hsu YP, Hesse LE, Beavers WN, Chazin WJ, Trinidad JC, VanNieuwenhze MS, Giedroc DP, Skaar EP. 2019. An Acinetobacter baumannii, zinc-regulated peptidase maintains cell wall integrity during immune-mediated nutrient sequestration. Cell Rep 26:2009–2018.e6. https://doi.org/10.1016/j.celrep.2019.01.089.

19. Glauner B, Holtje JV, Schwarz U. 1988. The composition of the murein of Escherichia coli. J Biol Chem 263:10088–10095. https://doi.org/10.1016/S0021-9258(19)81481-3.

20. Takacs CN, Hocking J, Cabeen MT, Bui NK, Poggio S, Vollmer W, Jacobs-Wagner C. 2013. Growth medium-dependent glycine incorporation into the peptidoglycan of Caulobacter crescentus. PLoS One 8:e57579. https://doi.org/10.1371/journal.pone.0057579.

21. Valbuena FM, Fitzgerald I, Strack RL, Andruska N, Smith L, Glick BS. 2020. A photostable monomeric superfolder green fluorescent protein. Traffic 21:534–544. https://doi.org/10.1111/tra.12737.

22. Magnet S, Arbeloa A, Mainardi JL, Hugonnet JE, Fourgeaud M, Dubost L, Marie A, Delfosse V, Mayer C, Rice LB, Arthur M. 2007. Specificity of L,D-transpeptidases from gram-positive bacteria producing different peptidoglycan chemotypes. J Biol Chem 282:13151–13159. https://doi.org/10.1074/jbc.M610911200.

23. Sycuro LK, Rule CS, Petersen TW, Wyckoff TJ, Sessler T, Nagarkar DB, Khalid F, Pincus Z, Biboy J, Vollmer W, Salama NR. 2013. Flow cytometry-based enrichment for cell shape mutants identifies multiple genes that influence Helicobacter pylori morphology. Mol Microbiol 90:869–883. https://doi.org/10.1111/mmi.12405.

24. Knight D, Dimitrova DD, Rudin SD, Bonomo RA, Rather PN. 2016. Mutations decreasing intrinsic beta-lactam resistance are linked to cell division in the nosocomial pathogen Acinetobacter baumannii. Antimicrob Agents Chemother 60:3751–3758. https://doi.org/10.1128/AAC.00361-16.

25. Malinverni JC, Silhavy TJ. 2009. An ABC transport system that maintains lipid asymmetry in the gram-negative outer membrane. Proc Natl Acad Sci U S A 106:8009–8014. https://doi.org/10.1073/pnas.0903229106.

26. Powers MJ, Trent MS. 2019. Intermembrane transport: glycerophospholipid homeostasis of the Gram-negative cell envelope. Proc Natl Acad Sci U S A 116:17147–17155. https://doi.org/10.1073/pnas.1902026116.

27. Bai J, Dai Y, Farinha A, Tang AY, Syal S, Vargas-Cuebas G, van Opijnen T, Isberg RR, Geisinger E. 2021. Essential gene analysis in Acinetobacter baumannii by high-density transposon mutagenesis and CRISPR interference. J Bacteriol 203:e00565-20. https://doi.org/10.1128/JB.00565-20.

28. Peters JM, Silvis MR, Zhao D, Hawkins JS, Gross CA, Qi LS. 2015. Bacterial CRISPR: accomplishments and prospects. Curr Opin Microbiol 27:121–126. https://doi.org/10.1016/j.mib.2015.08.007.

29. Klobucar K, Brown ED. 2018. Use of genetic and chemical synthetic lethality as probes of complexity in bacterial cell systems. FEMS Microbiol Rev 42. https://doi.org/10.1093/femsre/fux054.

30. Potluri LP, Kannan S, Young KD. 2012. ZipA is required for FtsZ-dependent preseptal peptidoglycan synthesis prior to invagination during cell division. J Bacteriol 194:5334–5342. https://doi.org/10.1128/JB.00859-12.

31. Pazos M, Peters K, Casanova M, Palacios P, VanNieuwenhze M, Breukink E, Vicente M, Vollmer W. 2018. Z-ring membrane anchors associate with cell wall synthases to initiate bacterial cell division. Nat Commun 9:5090. https://doi.org/10.1038/s41467-018-07559-2.

32. Hromas R, Kim HS, Sidhu G, Williamson E, Jaiswal A, Totterdale TA, Nole J, Lee SH, Nickoloff JA, Kong KY. 2017. The endonuclease EEPD1 mediates synthetic lethality in RAD52-depleted BRCA1 mutant breast cancer cells. Breast Cancer Res 19:122. https://doi.org/10.1186/s13058-017-0912-8.

33. Myers SH, Ortega JA, Cavalli A. 2020. Synthetic lethality through the lens of medicinal chemistry. J Med Chem 63:14151–14183. https://doi.org/10.1021/acs.jmedchem.0c00766.

34. Zinovyev A, Kuperstein I, Barillot E, Heyer WD. 2013. Synthetic lethality between gene defects affecting a single non-essential molecular pathway with reversible steps. PLoS Comput Biol 9:e1003016. https://doi.org/10.1371/journal.pcbi.1003016.

35. Park JT, Uehara T. 2008. How bacteria consume their own exoskeletons (turnover and recycling of cell wall peptidoglycan). Microbiol Mol Biol Rev 72:211–227. https://doi.org/10.1128/MMBR.00027-07.

36. Carroll SA, Hain T, Technow U, Darji A, Pashalidis P, Joseph SW, Chakraborty T. 2003. Identification and characterization of a peptidoglycan hydrolase, MurA, of Listeria monocytogenes, a muramidase needed for cell separation. J Bacteriol 185:6801–6808. https://doi.org/10.1128/JB.185.23.6801-6808.2003.

37. Borisova M, Gisin J, Mayer C. 2014. Blocking peptidoglycan recycling in Pseudomonas aeruginosa attenuates intrinsic resistance to fosfomycin. Microb Drug Resist 20:231–237. https://doi.org/10.1089/mdr.2014.0036.

38. Gil-Marques ML, Moreno-Martinez P, Costas C, Pachon J, Blazquez J, McConnell MJ. 2018. Peptidoglycan recycling contributes to intrinsic resistance to fosfomycin in Acinetobacter baumannii. J Antimicrob Chemother 73:2960–2968. https://doi.org/10.1093/jac/dky289.

39. Mainardi JL, Fourgeaud M, Hugonnet JE, Dubost L, Brouard JP, Ouazzani J, Rice LB, Gutmann L, Arthur M. 2005. A novel peptidoglycan cross-linking enzyme for a beta-lactam-resistant transpeptidation pathway. J Biol Chem 280:38146–38152. https://doi.org/10.1074/jbc.M507384200.

40. Htoo HH, Brumage L, Chaikeeratisak V, Tsunemoto H, Sugie J, Tribuddharat C, Pogliano J, Nonejuie P. 2019. Bacterial cytological profiling as a tool to study mechanisms of action of antibiotics that are active against Acinetobacter baumannii. Antimicrob Agents Chemother 63:e02310-18. https://doi.org/10.1128/AAC.02310-18.

41. Biarrotte-Sorin S, Hugonnet JE, Delfosse V, Mainardi JL, Gutmann L, Arthur M, Mayer C. 2006. Crystal structure of a novel beta-lactam-insensitive peptidoglycan transpeptidase. J Mol Biol 359:533–538. https://doi.org/10.1016/j.jmb.2006.03.014.

42. Marchler-Bauer A, Bo Y, Han L, He J, Lanczycki CJ, Lu S, Chitsaz F, Derbyshire MK, Geer RC, Gonzales NR, Gwadz M, Hurwitz Dl, Lu F, Marchler GH, Song JS, Thanki N, Wang Z, Yamashita RA, Zhang D, Zheng C, Geer LY, Bryant SH. 2017. CDD/SPARCLE: functional classification of proteins via subfamily domain architectures. Nucleic Acids Res 45:D200–D203. https://doi.org/10.1093/nar/gkw1129.

43. Sandoz KM, Popham DL, Beare PA, Sturdevant DE, Hansen B, Nair V, Heinzen RA. 2016. Transcriptional profiling of Coxiella burnetii reveals extensive cell wall remodeling in the small cell variant developmental form. PLoS One 11:e0149957. https://doi.org/10.1371/journal.pone.0149957.

44. Begg KJ, Takasuga A, Edwards DH, Dewar SJ, Spratt BG, Adachi H, Ohta T, Matsuzawa H, Donachie WD. 1990. The balance between different peptidoglycan precursors determines whether Escherichia coli cells will elongate or divide. J Bacteriol 172:6697–6703. https://doi.org/10.1128/jb.172.12.6697-6703.1990.

45. Markiewicz Z, Broome-Smith JK, Schwarz U, Spratt BG. 1982. Spherical E. coli due to elevated levels of D-alanine carboxypeptidase. Nature 297:702–704. https://doi.org/10.1038/297702a0.

46. Truong TT, Vettiger A, Bernhardt TG. 2020. Cell division is antagonized by the activity of peptidoglycan endopeptidases that promote cell elongation. Mol Microbiol 114:966–978. https://doi.org/10.1111/mmi.14587.

47. Botta GA, Park JT. 1981. Evidence for involvement of penicillin-binding protein 3 in murein synthesis during septation but not during cell elongation. J Bacteriol 145:333–340. https://doi.org/10.1128/jb.145.1.333-340.1981.

48. Pisabarro AG, Prats R, Vaquez D, Rodriguez-Tebar A. 1986. Activity of penicillin-binding protein 3 from Escherichia coli. J Bacteriol 168:199–206. https://doi.org/10.1128/jb.168.1.199-206.1986.

49. Powers MJ, Trent MS. 2018. Phospholipid retention in the absence of asymmetry strengthens the outer membrane permeability barrier to last-resort antibiotics. Proc Natl Acad Sci U S A 115:E8518–E8527. https://doi.org/10.1073/pnas.1806714115.

50. Baarda BI, Zielke RA, Le Van A, Jerse AE, Sikora AE. 2019. Neisseria gonorrhoeae MlaA influences gonococcal virulence and membrane vesicle production. PLoS Pathog 15:e1007385. https://doi.org/10.1371/journal.ppat.1007385.

51. Roier S, Zingl FG, Cakar F, Durakovic S, Kohl P, Eichmann TO, Klug L, Gadermaier B, Weinzerl K, Prassl R, Lass A, Daum G, Reidl J, Feldman MF, Schild S. 2016. A novel mechanism for the biogenesis of outer membrane vesicles in Gram-negative bacteria. Nat Commun 7:10515. https://doi.org/10.1038/ncomms10515.

52. Rojas ER, Billings G, Odermatt PD, Auer GK, Zhu L, Miguel A, Chang F, Weibel DB, Theriot JA, Huang KC. 2018. The outer membrane is an essential

load-bearing element in Gram-negative bacteria. Nature 559:617–621. https://doi.org/10.1038/s41586-018-0344-3.

53. Korza HJ, Bochtler M. 2005. Pseudomonas aeruginosa LD-carboxypepti-dase, a serine peptidase with a Ser-His-Glu triad and a nucleophilic elbow. J Biol Chem 280:40802–40812. https://doi.org/10.1074/jbc.M506328200.

54. Hoyland CN, Aldridge C, Cleverley RM, Duchene MC, Minasov G, Onopriyenko O, Sidiq K, Stogios PJ, Anderson WF, Daniel RA, Savchenko A, Vollmer W, Lewis RJ. 2014. Structure of the LdcB LD-carboxypeptidase reveals the molecular basis of peptidoglycan recognition. Structure 22:949–960. https://doi.org/10.1016/j.str.2014.04.015.

55. Mainardi JL, Hugonnet JE, Rusconi F, Fourgeaud M, Dubost L, Moumi AN, Delfosse V, Mayer C, Gutmann L, Rice LB, Arthur M. 2007. Unexpected in-hibition of peptidoglycan LD-transpeptidase from Enterococcus faecium by the beta-lactam imipenem. J Biol Chem 282:30414–30422. https://doi.org/10.1074/jbc.M704286200.

56. Choi KH, Kumar A, Schweizer HP. 2006. A 10-min method for preparation of highly electrocompetent Pseudomonas aeruginosa cells: application for DNA fragment transfer between chromosomes and plasmid transfor-mation. J Microbiol Methods 64:391–397. https://doi.org/10.1016/j.mimet.2005.06.001.

57. Geisinger E, Isberg RR. 2015. Antibiotic modulation of capsular exopoly-saccharide and virulence in Acinetobacter baumannii. PLoS Pathog 11:e1004691. https://doi.org/10.1371/journal.ppat.1004691.

58. Geisinger E, Mortman NJ, Vargas-Cuebas G, Tai AK, Isberg RR. 2018. A global regulatory system links virulence and antibiotic resistance to enve-lope homeostasis in Acinetobacter baumannii. PLoS Pathog 14:e1007030. https://doi.org/10.1371/journal.ppat.1007030.

59. Guzzo M, Castro LK, Reisch CR, Guo MS, Laub MT. 2020. A CRISPR interfer-ence system for efficient and rapid gene knockdown in Caulobacter cres-centus. mBio 11:e02415-19. https://doi.org/10.1128/mBio.02415-19.

60. Qi LS, Larson MH, Gilbert LA, Doudna JA, Weissman JS, Arkin AP, Lim WA. 2013. Repurposing CRISPR as an RNA-guided platform for sequence-spe-cific control of gene expression. Cell 152:1173–1183. https://doi.org/10.1016/j.cell.2013.02.022.

61. Carruthers MD, Nicholson PA, Tracy EN, Munson RS, Jr. 2013. Acineto-bacter baumannii utilizes a type VI secretion system for bacterial compe-tition. PLoS One 8:e59388. https://doi.org/10.1371/journal.pone.0059388.

62. Kumar A, Dalton C, Cortez-Cordova J, Schweizer HP. 2010. Mini-Tn7 vec-tors as genetic tools for single copy gene cloning in Acinetobacter bau-mannii. J Microbiol Methods 82:296–300. https://doi.org/10.1016/j.mimet.2010.07.002.

63. Jacobs AC, Thompson MG, Black CC, Kessler JL, Clark LP, McQueary CN, Gancz HY, Corey BW, Moon JK, Si Y, Owen MT, Hallock JD, Kwak YI, Summers A, Li CZ, Rasko DA, Penwell WF, Honnold CL, Wise MC, Waterman PE, Lesho EP, Stewart RL, Actis LA, Palys TJ, Craft DW, Zurawski DV. 2014. AB5075, a highly virulent isolate of Acinetobacter baumannii, as a model strain for the evaluation of pathogenesis and antimicrobial treatments. mBio 5:e01076-14. https://doi.org/10.1128/mBio.01076-14.

64. Geisinger E, Vargas-Cuebas G, Mortman NJ, Syal S, Dai Y, Wainwright EL, Lazinski D, Wood S, Zhu Z, Anthony J, van Opijnen T, Isberg RR. 2019. The landscape of phenotypic and transcriptional responses to ciprofloxacin in Acinetobacter baumannii: acquired resistance alleles modulate drug-induced SOS response and prophage replication. mBio 10:e01127-19. https://doi.org/10.1128/mBio.01127-19.

65. DeJesus MA, Ambadipudi C, Baker R, Sassetti C, Ioerger TR. 2015. TRANSIT: a software tool for Himar1 TnSeq analysis. PLoS Comput Biol 11:e1004401. https://doi.org/10.1371/journal.pcbi.1004401.

66. Robinson JT, Thorvaldsdottir H, Winckler W, Guttman M, Lander ES, Getz G, Mesirov JP. 2011. Integrative genomics viewer. Nat Biotechnol 29:24–26. https://doi.org/10.1038/nbt.1754.

67. Schindelin J, Arganda-Carreras I, Frise E, Kaynig V, Longair M, Pietzsch T, Preibisch S, Rueden C, Saalfeld S, Schmid B, Tinevez JY, White DJ, Hartenstein V, Eliceiri K, Tomancak P, Cardona A. 2012. Fiji: an open-source platform for biological-image analysis. Nat Methods 9:676–682. https://doi.org/10.1038/nmeth.2019.

68. Ducret A, Quardokus EM, Brun YV. 2016. MicrobeJ, a tool for high throughput bacterial cell detection and quantitative analysis. Nat Micro-biol 1:16077. https://doi.org/10.1038/nmicrobiol.2016.77.

69. Schneider CA, Rasband WS, Eliceiri KW. 2012. NIH Image to ImageJ: 25 years of image analysis. Nat Methods 9:671–675. https://doi.org/10.1038/nmeth.2089.

70. van Opijnen T, Bodi KL, Camilli A. 2009. Tn-seq: high-throughput parallel sequencing for fitness and genetic interaction studies in microorganisms. Nat Methods 6:767–772. https://doi.org/10.1038/nmeth.1377.

71. Alvarez L, Hernandez SB, de Pedro MA, Cava F. 2016. Ultra-sensitive, high-resolution liquid chromatography methods for the high-throughput quantitative analysis of bacterial cell wall chemistry and structure. Meth-ods Mol Biol 1440:11–27. https://doi.org/10.1007/978-1-4939-3676-2_2.

72. Deatherage DE, Barrick JE. 2014. Identification of mutations in labora-tory-evolved microbes from next-generation sequencing data using breseq. Methods Mol Biol 1151:165–188. https://doi.org/10.1007/978-1-4939-0554-6_12.

73. Choi Y, Sims GE, Murphy S, Miller JR, Chan AP. 2012. Predicting the func-tional effect of amino acid substitutions and indels. PLoS One 7:e46688. https://doi.org/10.1371/journal.pone.0046688.

74. Siguier P, Perochon J, Lestrade L, Mahillon J, Chandler M. 2006. ISfinder: the reference centre for bacterial insertion sequences. Nucleic Acids Res 34:D32–D36. https://doi.org/10.1093/nar/gkj014.

75. Coyle JF, Pagliai FA, Zhang D, Lorca GL, Gonzalez CF. 2018. Purification and par-tial characterization of LdtP, a cell envelope modifying enzyme in Liberibacter asiaticus. BMC Microbiol 18:201. https://doi.org/10.1186/s12866-018-1348-8.

76. Markiewicz Z, Glauner B, Schwarz U. 1983. Murein structure and lack of DD- and LD-carboxypeptidase activities in Caulobacter crescentus. J Bac-teriol 156:649–655. https://doi.org/10.1128/jb.156.2.649-655.1983.

77. Almagro Armenteros JJ, Tsirigos KD, Sonderby CK, Petersen TN, Winther O, Brunak S, von Heijne G, Nielsen H. 2019. SignalP 5.0 improves signal peptide predictions using deep neural networks. Nat Biotechnol 37:420–423. https://doi.org/10.1038/s41587-019-0036-z.

78. Hiller K, Grote A, Scheer M, Munch R, Jahn D. 2004. PrediSi: prediction of signal peptides and their cleavage positions. Nucleic Acids Res 32:W375–W379. https://doi.org/10.1093/nar/gkh378.

79. Kall L, Krogh A, Sonnhammer EL. 2007. Advantages of combined transmem-brane topology and signal peptide prediction: the Phobius web server. Nucleic Acids Res 35:W429–32. https://doi.org/10.1093/nar/gkm256.

80. Krogh A, Larsson B, von Heijne G, Sonnhammer EL. 2001. Predicting trans-membrane protein topology with a hidden Markov model: application to complete genomes. J Mol Biol 305:567–580. https://doi.org/10.1006/jmbi.2000.4315.